Mathematical Biosciences 374 (2024) 109219

Contents lists available at ScienceDirect

Mathematical Biosciences

journal homepage: www.elsevier.com/locate/mbs

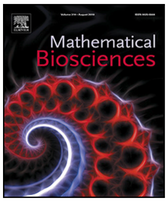

Original Research Article

A theoretical model of anaphase

Brian D. Sleeman[a], Iain W. Stewart[b,*]

[a] School of Mathematics, University of Leeds, Leeds, LD2 9JT, United Kingdom
[b] Department of Mathematics and Statistics, University of Strathclyde, Livingstone Tower, 26 Richmond Street, Glasgow, G1 1XH, United Kingdom

ARTICLE INFO

MSC:
92C37
92-10
76A15

Keywords:
Anaphase
Nematic liquid crystal
Defects
Dafermos energy
Cytoplasm
Microtubules
Regions of influence
HeLa cell
Caenorhabditis elegans

ABSTRACT

This paper develops a theory for anaphase in cells. After a brief description of microtubules, the mitotic spindle and the centrosome, a mathematical model for anaphase is introduced and developed in the context of the cell cytoplasm and liquid crystalline structures. Prophase, prometaphase and metaphase are then briefly described in order to focus on anaphase, which is the main study of this paper. The entities involved are modelled in terms of liquid crystal defects and microtubules are represented as defect flux lines. The mathematical techniques employed make extensive use of energy considerations based on the work that was developed by Dafermos (1970) from the classical Frank–Oseen nematic liquid crystal energy (Frank, 1958; Oseen, 1933). With regard to liquid crystal theory we introduce the concept of *regions of influence* for defects which it is believed have important implications beyond the subject of this paper. The results of this paper align with observed biochemical phenomena and are explored in application to HeLa cells and Caenorhabditis elegans. This unified approach offers the possibility of gaining insight into various consequences of mitotic abnormalities which may result in Down syndrome, Hodgkin lymphoma, breast, prostate and various other types of cancer.

1. Introduction

Mitosis is an orchestrated series of events which allow the chromosomes within the nucleus of all living cells to duplicate and reposition themselves in readiness for cytokinesis (cell division). Other components of the cell, including mitochondria, cytosol etc., are also subject to analogous processes. The molecular biology of mitosis is extremely well studied [1]. It has also been observed for well over a century [2] that the cytoplasm of the cell appears to behave as a nematic liquid crystal. However it is only within the last fifty years that developments in the theory of liquid crystals have opened up new ways to begin to understand the interconnected sequences of events involved in cell mitosis and cytokinesis. Liquid crystals can be thought of as generally consisting of elongated rod-like molecules which have a preferred local average direction. In the nematic liquid crystal phase the long axes of these constituent molecules align parallel to each other along some common preferred direction, usually denoted by the unit vector $\mathbf{n}(\mathbf{x},t)$, called the director. This direction is often called the anisotropic axis and is indicative of the alignment of the constituent material at a given location $\mathbf{x}$ at time t. It is such alignment directions that can be linked to models of aligning materials in cell biology. Examples of alignment directions are shown in more detail in Figs. 4 and 5 and discussed below, where they are referred to as 'flux lines' which are tangential to the director $\mathbf{n}$ within the aligning materials. More details on the physics and mathematical descriptions of liquid crystals can be found in books [3–6] and the reviews in [7,8].

Illustrations of cells and schematics of their structure can be found in the textbook by Alberts et al. [1]. As a cell contains many different structures and organelles it is currently impossible to incorporate all components of a cell in this theory. Instead we concentrate on the mitotic roles of the main players in anaphase, namely the cytoplasm, microtubules, chromatids and the centrosome. In Section 2 we briefly describe these entities and mention the prophase, prometaphase and metaphase as precursors to the fourth phase of cell mitosis known as anaphase, which is the main area of focus in this paper. Section 3 provides a description of chromatids, microtubules and the centrosome in the context of nematic liquid crystal defects and introduces the concept of regions of influence in relation to these structures; the interpretation of 'defect' in this context is briefly highlighted in Section 2.1. A summary of the construction of the nematic defect interaction energy using the director $\mathbf{n}$ is given in Appendix A. This provides the impetus for the key novel mathematical modelling aspects of anaphase that are developed in Section 4 with model examples given for HeLa cells and Caenorhabditis elegans cells (C. elegans) explored in Section 5; we compare our theoretical results with data obtained from the literature for these cell types. The paper closes in Section 6 with some conclusions and future directions.

---

* Corresponding author.
E-mail address: i.w.stewart@strath.ac.uk (I.W. Stewart).

https://doi.org/10.1016/j.mbs.2024.109219
Received 1 February 2024; Received in revised form 2 May 2024; Accepted 20 May 2024

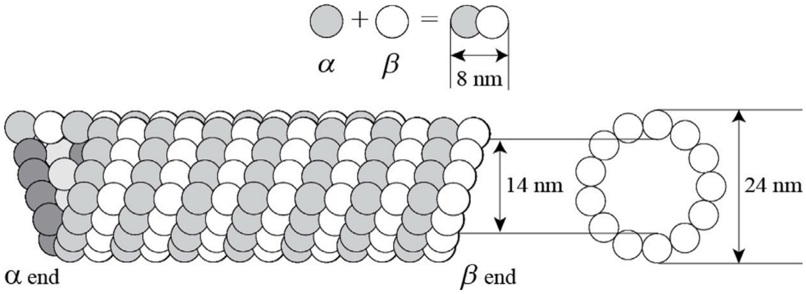

Fig. 1. A schematic diagram of a microtubule cylinder based on that presented in [9, p. 564] and [10] with approximate dimensions for its inner and outer radii. The wall of the microtubule consists of α and β tubulin heterodimers as shown. The cross-section shows an end view with the standard arrangement of thirteen heterodimers.

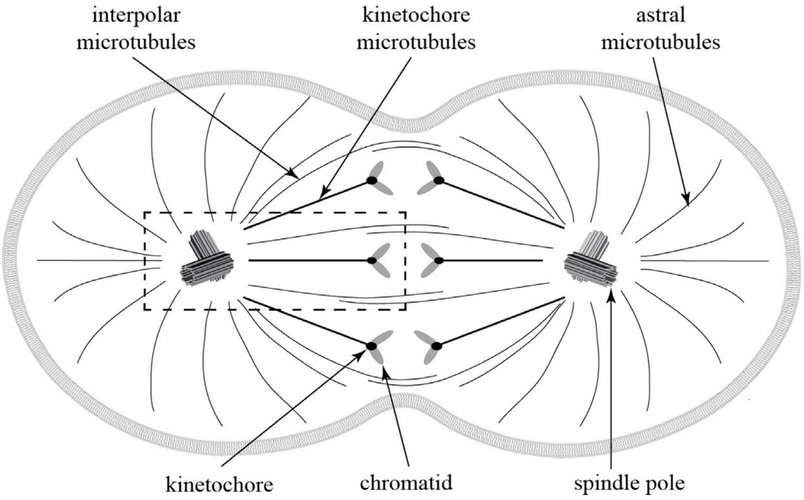

Fig. 2. A schematic diagram of the structure of the mitotic spindle which consists of various types of microtubules that are involved in mitosis. This figure is based upon the representation given in the eBook by O'Connor et al. [11]. The centrosome (see Fig. 3) placed at a spindle pole, kinetochore microtubules connected to the kinetochore and chromatid contained within the dashed rectangle are related to the three Frank nematic liquid crystal defects pictured in Fig. 4; the bold line connected to the kinetochore can consist of a single or multiple microtubules aligned parallel to form a kinetochore fibre and the number of such placed microtubules depends on the cell type.

2. Microtubules, mitotic spindle, centrosome, prophase, prometaphase, metaphase

2.1. Microtubules and the mitotic spindle

Cytoplasm is the material under the cell membrane but exterior to the cell nucleus and consists of a gel-like substance called cytosol, an internal substructure of organelles and various cytoplasmic inclusions. Among these inclusions are microtubules, which are present in the cells of all multicellular organisms, which are cylinders formed by polymeric strands of tubulin. To be specific, microtubules are formed by the polymerisation of dimers of two homologous proteins, α and β tubulin, to form heterodimers of approximately 8 nm in length as displayed in Fig. 1. They occur throughout the cytoplasm of the cell and are major components of the cell. Microtubules, shown in Fig. 1, are dynamic and they are continually growing and shrinking. They are crucial in establishing the mitotic spindle, shown in Fig. 2, and in chromosome separation. The spindle becomes almost invisible as the microtubules disintegrate, a property called microtubule 'catastrophe'. The growth and shrinkage of a microtubule is dependent on the concentration of α and β tubulin subunits. To maintain the rate of gain at the β end (plus end) and the erosion of the α end (minus end), a process called 'steady state treadmilling' is invoked and to maintain this steady state a constant energy input is required. It is in this context that microtubules, as we shall see, can be considered as flux lines of liquid crystal defects (see Appendix A and Figs. 2, 4 and 5).

Note that the term 'defect' is a standard terminology throughout the liquid crystal literature. Despite this, in the context here, the material that occupies the core at the centre of a defect structure, such as a spindle pole, chromatid, etc., will be considered as an object with mass that occupies a physical volume of space; in the simplest liquid crystal defects such structures are presumed to have zero mass at the core, and the energies used to model them are often modelled by replacing the actual core by a void of radius r_c, called the core radius [5], usually estimated to be of the order of molecular dimensions [4, p. 171]. This is not required in the model presented here since, for example, we can absorb and exploit the core mass of a spindle pole as part of the model; nevertheless, the idea of a core radius remains, the difference being that here the core is no longer a void.

A cell with its mitotic spindle undergoing mitosis is shown in Fig. 2 where schematically some chromatids, each with their own kinetochore drawn as a bold circle which is attached to its associated kinetochore microtubule drawn as a bold line, are pictured. Each of the bold lines connected to the kinetochores in Fig. 2 can consist of a single microtubule or multiple microtubules aligned parallel to form a kinetochore fibre. The number of such aligned microtubules that make up each kinetochore fibre is dictated by the cell type. For example, 1 microtubule in budding yeast, 3 or 4 microtubules in fission yeast, up to 20 to 30 microtubules in human cells [12]. The two spindle poles each consist of a centrosome which is described below in greater detail in Fig. 3. There are other microtubules involved in mitosis and interpolar and astral microtubules are also shown schematically for information. The area within the dashed rectangle in Fig. 2 will be the focus of our attention as representative of anaphase behaviour that will be occurring for each such kinetochore fibre and its associated kinetochore and chromatid. The centrosome at a spindle pole, the kinetochore fibre and

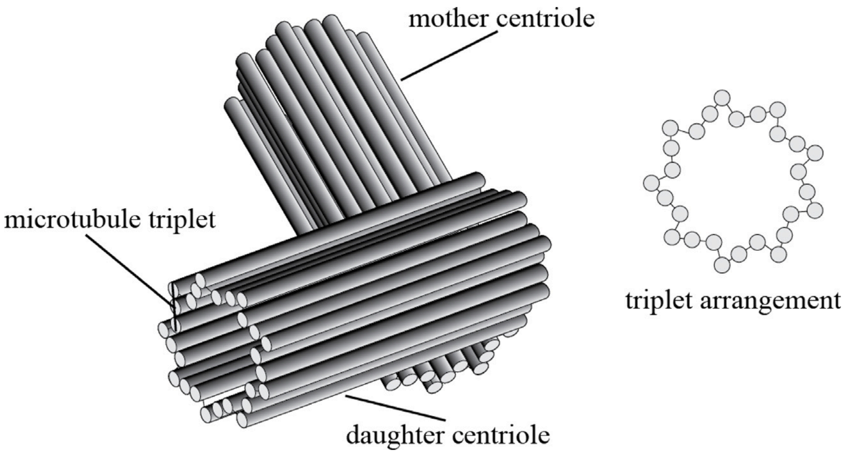

Fig. 3. The centrosome is composed of two centrioles made up of microtubules as shown. The cross-section shows the nine triplet arrangement of the twenty-seven microtubules in each centriole.

the chromatid with its kinetochore will be described in terms of liquid crystal defect structures in Section 3. This will form the basis for the model of anaphase.

2.2. The centrosome

A central player in mitosis is the centriole which is a cylindrical organelle composed mainly of tubulin. A centriole is typically made up of nine sets of short tubulin triplets arranged in the cylindrical structure shown in Fig. 3.

Before replication of the DNA within the nucleus, the cell contains two centrioles, a mother centriole and a daughter centriole which are positioned orthogonally adjacent to one another to form the centrosome. During the cell division cycle, a new centriole pair grows at the proximal end of both mother and daughter centrioles. After this duplication the new centrosome remains attached to the parent until the onset of prophase.

Within a cell, the centrosome is located outside but near the nucleus. Its precise positioning is fundamental to the orchestration of the mitotic process. It has recently been reported [13,14] that the protein Casein kinase 1a ($CK1\alpha$) localises to the centriole pair and is required for its proper positioning and subsequent dynamics. $CK1\alpha$ is recruited by the protein Family with Sequence Similarity 83 Member D ($FAM83D$) and the absence of $FAM83D$ in cells leads to pronounced centriole positioning which leads to defective mitosis and may be implicated in pre-leukaemic myelodysplastic syndrome and other cancers. The dynamic positioning of the centriole will be modelled during anaphase and we speculate that adapting this model may enable defective mitosis to be investigated in future work.

2.3. Prophase, prometaphase and metaphase

This subsection describes briefly some elements of mitosis. Further details can be found in [1].

Prophase is the first stage of mitosis whereby the complex of DNA and proteins within the nucleus, referred to as chromatin, condenses. The chromatin coils up and becomes compact resulting in the formation of chromosomes. Each chromosome is made up of a single strand of highly organised DNA. The chromosomes then replicate themselves and have a visibly distinctive X shape and are called sister chromatids. Chromatids are thus pairs of identical copies of DNA joined at a central point called the centromere. At the initiation of prophase microtubules which form part of the cell's cytoskeleton disassemble to form a pool of tubulin molecules. These molecules are recruited to form the mitotic spindle. This microstructure then focuses on the centriole to become the mitotic centre. The centriole together with a radial array of microtubules, known as astral microtubules, is called the aster [1, p. 931]. The astral microtubules have their α ends embedded in the centrosome. The cell's original aster then replicates to form two asters which push apart to result in a bipolar mitotic spindle as shown in Fig. 2 with the asters forming the cores of two spindle poles.

During prometaphase, which is the second stage of mitosis, dynamic instability allows astral microtubules to search efficiently in space, probing the spindle volume until they capture chromosomes by binding to their kinetochores, a search and capture process (see Fig. 2). The centrosomes move towards the opposite ends of the spindle pole.

Metaphase is the third stage of mitosis in which a lipid bilayer interface forms along the equatorial plane, a vertical plane that would be located in the centre of Fig. 2, called the metaphase plate. During this phase the mitotic spindle becomes fully developed as shown in Fig. 2.

The fourth phase of mitosis is anaphase. Anaphases A and B are our main concern and will be investigated in Section 4. In order to proceed, descriptions of defects in the context of mitosis, and the novel use of regions of influence, will be introduced in the next section.

3. Defects and regions of influence

The highly concentrated and localised reorientation regions within the cytoplasm (cf. Fig. 2) can be considered in the context of defects. Such core defects, represented by central solid circles in Fig. 4 have a physical location, magnitude and mass. We can represent these cores as circles of a given fixed radius r_0. A mathematical review of the defects in Fig. 4, and other classical Frank defects, can be found in [5] and within the wider general context of defects and textures in [3,4,15].

Throughout the modelling of mitosis and cytokinesis, microtubules play a fundamental role. For example, in prophase the mitotic spindle pole may be modelled as a $+1$ Frank defect (see Fig. 4) which in the Frank–Oseen theory of nematic liquid crystals has an energy density w proportional to the inverse square of the distance r from its core centre. That is, ω is proportional to $1/r^2$ which implies the energy density is infinite at the centre of the core. However, in our theory the core $0 \leq r \leq r_0$, for some $r_0 > 0$, is occupied by the centrosome or other proteins at the core of a defect and therefore such singular behaviour is absent in this situation. In addition it is also the case that the total free energy over a region of radius R is proportional to $\ln(R/r_0)$ which again becomes infinite as $R \to \infty$, although at a slow growth rate. When considering the free energy density of the interaction of two defects, it is usually assumed that interaction occurs between defects regardless of the inter-core centre distance. This would imply, for example in prophase, that the microtubules forming the

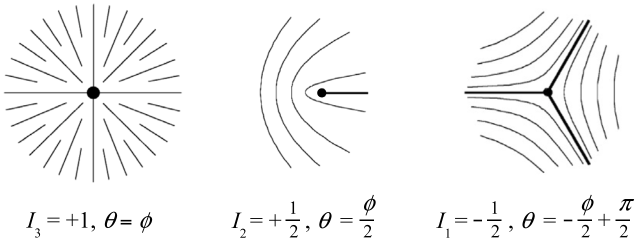

Fig. 4. Graphs of 'flux lines' which are tangential to the orientation of the aligning constituents. A central dot in each figure represents the location of a defect core of index (strength) $I = n/2$ where n is the classical Frank index. With the exception of the case for $I_3 = +1$, the bold lines represent singular radial lines that emanate from the core, as described in Appendix A together with a description of the alignment angle θ and polar coordinate angle ϕ. These three defects are basic to the modelling within the dashed rectangular box shown in Fig. 2.

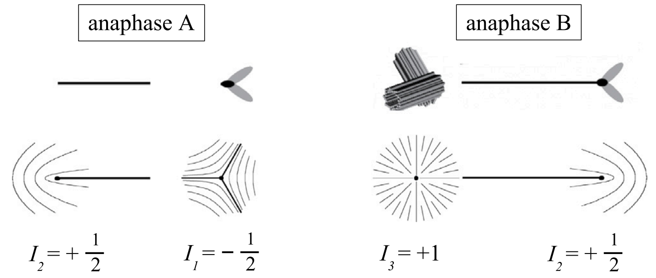

Fig. 5. The main model structures for anaphase A and anaphase B. In anaphase A a chromatid with its kinetochore and its associated MAP$^+$ are represented as attractive defects $I_1 = -1/2$ and $I_2 = +1/2$ of opposite sign with masses m_1 and m_2, respectively. In anaphase B the centrosome is represented by the defect $I_3 = +1$ with mass m_3 while its associated combination of MAP$^+$ and its captured chromatid are represented as a revised defect structure $I_2 = +1/2$ with revised mass $m_{22} = m_1 + m_2$; these defects of the same sign will repel each other and induce the dynamics of anaphase B.

mitotic spindle have influence throughout the whole cytoplasm. We believe this to be unreasonable during anaphase and postulate that associated with each defect I_j there is a *region of influence*[1] Ω_j, which could be, in two dimensions, an enclosed area of a given shape that surrounds I_j. For example, two neighbouring defects I_1 and I_2 could each have a circular region of influence of radii R_1 and R_2, respectively, and interaction can only occur where R_1 and R_2 overlap to form a non-empty intersecting region $R_{intersect} = R_1 \cap R_2$; this concept will be developed in greater detail in Section 4. A similar approach could be taken for rectangles or combinations of regions with different shapes. In Appendix A, where the interaction energy density is considered, it is assumed that the constituent regions of influence have a common intersection. Outside such regions the interaction energy density is simply the sum of individual densities. In practice, regions of influence may well be dynamic and evolve with time. Furthermore, rather than being described by circles, as here, they will adopt different topologies depending on the types of defect. For simplicity in this elementary approach we assume circular regions of influence of fixed radii throughout this paper; time-dependent regions of variable shape can be accommodated as part of the modelling which is much beyond the scope of this novel first investigation using regions of influence.

It should be noted that the +1/2 and −1/2 Frank defects shown in Fig. 4 have previously been considered in [17, Fig. 2] for the patterning and collective motion of neural progenitor cells and in [18] for a description of active nematic liquid crystals in the context of cellular arrangements (see also the comments in [19]). It should also be mentioned that +1 defects in nematic liquid crystals have been used in [20] for a confined geometry which models centrioles in a basic description of a cell undergoing cell division, an approach which necessarily deploys different modelling assumptions to those used in this paper.

We close this section with some crucially important observations. Firstly, the three defects shown in Fig. 4 will model the regions focused around a spindle core. A typical kinetochore microtubule fibre and its 'captured' chromatid is, for example, displayed within the dotted rectangle in Fig. 2. Such an approach will enable a direct mathematical description of anaphase that deploys these three key entities within the mitotic spindle. As detailed in the next section, defects of the same sign repel each other while defects of opposite sign are attracted to each other. A schematic of our approach is displayed in Fig. 5. Anaphase A is modelled as a two-body problem where the $I_1 = -1/2$ defect represents a typical chromatid with a core mass m_1 that is mutually attracted to a defect $I_2 = +1/2$ which represents a MAP$^+$ core of mass m_2 within a kinetochore fibre (details below in Section 5.1). The force of attraction between the chromatid and the MAP$^+$ induces the dynamics and this is what is mathematically modelled Sections 4 and 5. A similar approach is used to model the dynamics of anaphase B when the centrosome is modelled as a defect $I_3 = +1$ with mass m_3 while the combination of the MAP$^+$ and its captured chromatid are set as a revised defect structure $I_2 = +1/2$ with a revised mass $m_{22} = m_1 + m_2$. The repulsive force between these defects drives their motion. The examples explored in Section 5 for a HeLa cell and a C. elegans cell will examine anaphase A followed by anaphase B and discuss the results.

Secondly, schematic figures of liquid crystal defects in two dimensions, such as those depicted in Fig. 5, set within the context of general cells, can be found in the short review by Mogilner et al. [21] and, as mentioned above, the descriptions provided by Leoni et al. [20]. Of more direct, and recent, interest to this present article is the short review on the physics of liquid crystals in cell biology by Doostmohammadi and Ladoux [22] where liquid crystal defects of orders −1/2, +1/2 and +1 were interpreted in an identical way to those displayed here in Fig. 5, noting that there are three principal types of +1 defects, as shown in [5, p. 114]; microtubules are also discussed within the setting of localised topological liquid crystal defects in [22].

Thirdly, in this article and in all the aforementioned references, there are some modelling assumptions that allow a two-dimensional description of liquid crystal defects to be feasible in the modelling of cells; of course, a three-dimensional model would be ideal, but this is well beyond the scope of the models used here and in the aforementioned references. The first basic assumption throughout this common two-dimensional modelling is that the model reflects a relatively thin cross-section of a real cell. This assumption has successfully modelled phenomena in a straightforward way in the work of others in cell biology and in this article. Moreover, this assumption has been successful and widely deployed in the liquid crystal literature under similar modelling restrictions and has yielded valuable physical insights [3–7] which have motivated the use of Frank defects in cell biology and other areas. A second basic assumption for cell biology is that the defects are embedded in finite regions; in reality, the infinite regions originally used in the mathematical modelling approximate distances that reach beyond the molecular scale. A key novelty in this article is to exploit the finite range of these defects inside cells under the assumption that there will be finite regions of influence. Each defect will have its own finite range of biochemical interaction with nearby defects which also possess interactive ranges of influence. It is the biochemical interaction that occurs when these regions overlap that produces the attraction or repulsion between interacting defects. The size and shape of such regions of influence and their overlap is approximated here by circles

---

[1] This hypothesis may have been in the mind of Isaac Newton who wrote in his Opticks [16] in Query 31 "I had rather infer from their cohesian, that their particles attract one another by some force, which in immediate contact is exceeding strong, at small distances performs the chymical operations above mention'd, and reaches not far from the particles with any sensible effect".

in two dimensions with a ‘cylindrical height’ to aid calculations and modelling with some physical depth. Details on this methodology will be explored in the following two Sections. The sizes and shapes for regions of influence and their overlapping interaction areas will clearly be affected by the available area, or volume, of a confined cell shape and size. The finite regions of influence adopted below are circular as a first approximation; such regions and the methodology introduced here are key novel concepts which, to the best of our knowledge, have not been defined elsewhere and can be adapted to other differing shapes and sizes which are open to future exploration and investigation that is clearly beyond the reach of this first novel approach. How such regions are selected is yet to be fully investigated, but, as in other areas of related research in liquid crystals (referred to previously), a first approximation for them to be circular has been introduced for ease of exposition and numerical calculation.

4. Anaphase

During anaphase, the sister chromatids separate and move to opposite polar regions of the mitotic spindle. This process is distinguished by two temporal, possibly overlapping, events referred to as anaphase A and anaphase B respectively. The onset of anaphase A is marked by the abrupt and synchronous separation of sister chromatids due to the sudden degradation of cohesion complexes between sister chromatids. Daughter chromosomes move to opposite spindle polar regions as their kinetochore fibres shorten. Individual kinetochores bind multiple microtubules. Anaphase B is the process whereby opposite spindle poles move further away from each other.

As can be seen from Appendix A, a disclination (defect) of index I_j has a general energy density proportional to I_j^2/r_j^2 when we choose to associate with this energy density a circular region of influence $0 < r_j \le R_j$, with r_j defined in Eq. (A.17). From the result in equation (A.18) the interaction energy density of two defects of indexes I_1 and I_2 is proportional to the product $I_1 I_2$ and inversely proportional to the product $r_1 r_2$. Furthermore, any interaction between defects is only significant where regions of radius R_1 and R_2 overlap. Outside this interacting region the total energy of the defects is simply the sum of the individual defect energies. For defects of the same sign there is a repulsive force and the defects move apart, for as long as their respective core regions overlap, while for defects of opposite sign there is an attractive force and the defects move towards each other. In modelling anaphase, two avenues may be studied. Firstly, we can model anaphase A followed sequentially by anaphase B or, secondly, we can model both anaphase A and anaphase B simultaneously. In the former case this leads to a pair of two-body problems in which we exploit the energy contribution ω defined in Eq. (A.18) while in the latter we would have a three-body problem in which the form for ω in Eq. (A.19) can be employed. Here we shall concentrate on a pair of two-body problems.

The presence of the microtubule associated protein (MAP), which governs the shortening of a particular kinetochore binding microtubule, is represented by a defect of index $I_2 = +1/2$ situated within the kinetochore microtubule towards the end that is attracted to the kinetochore at a selected modelling distance that will be set in the examples below, which is also within the region of the centriole which has index $I_3 = +1$. Anaphase A is initiated when the region of influence of the MAP with index $I_2 = +1/2$ overlaps with the region of influence of the kinetochore with index $I_1 = -1/2$ which results in an attraction between these two defects until they eventually make contact with each other and thereby deposit the associated chromatid in the neighbourhood of the centriole. That is, the kinetochore fibre shortens and the chromatid bearing defect moves closer towards the vicinity of the centriole. This process is performed during anaphase A for each daughter chromatid. While the region of influence of the kinetochore defect is exhausted by the much larger region of influence of the MAP during this process, the residual annular region of the MAP defect will still overlap with that of the +1 centriole defect. Since these latter two defects have the same sign there is a resulting repulsive force which effectively drives then apart; this leads to the onset of anaphase B. The process of anaphase A followed by anaphase B, as described here, occurs simultaneously in the left half and right half of Fig. 2 and ultimately the two pole centrioles will also move further apart from each other.

Following the notation introduced in Appendix B, the schematic set-up in Fig. 5 and the mathematical description depicted in Fig. 6, we choose to set the $I_1 = -1/2$ kinetochore defect as particle P_1 with mass m_1 and position vector $\mathbf{r}_1$, the $I_2 = +1/2$ MAP defect as particle P_2 with mass m_2 and position vector $\mathbf{r}_2$ and the $I_3 = +1$ centriole defect as P_3, with mass m_3 and position vector $\mathbf{r}_3$. For simplicity, it will be assumed that these particles can be modelled in two dimensions and that the physical core radii of the defects in this instance can each be approximated by a circle having the same fixed core radius r_0. Each defect will also be assumed to have an associated circular region of influence R_i, $i = 1$ to 3, that controls its interaction with other defects when their regions of influence overlap with it. These regions will be modelled as corresponding circular areas Ω_i, $i = 1$ to 3. The core radii, the masses of these particles and their regions of influence can be approximated by the example data presented in Table 1, as appropriate for the examples that will be investigated.

We begin by modelling anaphase A as the first of the pair of two-body problems. Anaphase B will be the second two-body problem that follows on sequentially from anaphase A. The notation and equations that now follow are given in terms of the interaction between P_1 and P_2; anaphase B will be considered analogously in terms of a modified P_2 and P_3 with similar forms of equations, the key difference in the arising dynamics being due to the different masses, regions of influence and the relative signs and magnitudes of the defect indexes.

In Cartesian coordinates, for anaphase A we can set the centres of P_1 and P_2 to be at $\mathbf{r}_1 = (x_1, 0)$ and $\mathbf{r}_2 = (x_2, 0)$, respectively, relative to an arbitrary fixed origin $\mathbf{O}$ as shown in Fig. 6 and set $d = x_1 - x_2$, where we can, without loss of generality, assume $x_1 > x_2$. This corresponds to setting $\mathbf{r} \equiv \mathbf{r}_1 - \mathbf{r}_2 = (d, 0)$ in the notation of Appendix B. A general schematic of the geometrical set-up is shown in Fig. 6 where the distances d_1 and d_2 are introduced; additionally, it proves convenient to define two further distances d_{11} and d_{12} for ease of notation in calculations. These distances are defined in terms of d, the core radius r_0, R_1 and R_2 by

$$d = d_1 + d_2, \qquad R_1^2 - R_2^2 = d_1^2 - d_2^2, \tag{1}$$

and

$$d_1 = \frac{R_1^2 - R_2^2 + d^2}{2d}, \qquad d_2 = \frac{R_2^2 - R_1^2 + d^2}{2d}, \tag{2}$$

$$d_{11} = \frac{-R_1^2 + r_0^2 + d^2}{2d}, \qquad d_{12} = \frac{-R_2^2 + r_0^2 + d^2}{2d}. \tag{3}$$

The internal energy is that arising from the energy for two interacting defects based on the model introduced by Dafermos [23] and the results presented in [24] for general liquid crystal defects known as disclinations, as described in Appendix A. The corresponding defect interaction energy per unit depth in the z-direction is given by

$$W = \frac{1}{2} K \int_{\Omega} \omega \, dx \, dy, \tag{4}$$

where $K > 0$ is a Frank elastic constant and $\Omega = \Omega_1 \cap \Omega_2$ is the area of the intersection of the two regions of influence of the defects, which clearly depends on the locations of P_1 and P_2 as they interact, as pictured in Fig. 6. The contribution ω to this integrand is given in general by Eq. (A.18) in Appendix A. In this instance, we have

$$\omega = \frac{I_1^2}{r_1^2} + \frac{I_2^2}{r_2^2} + \frac{2 I_1 I_2}{r_1 r_2} \cos(\chi^1 - \chi^2), \tag{5}$$

where

$$r_i^2 = (x - x_i)^2 + y^2, \qquad i = 1, 2, \tag{6}$$

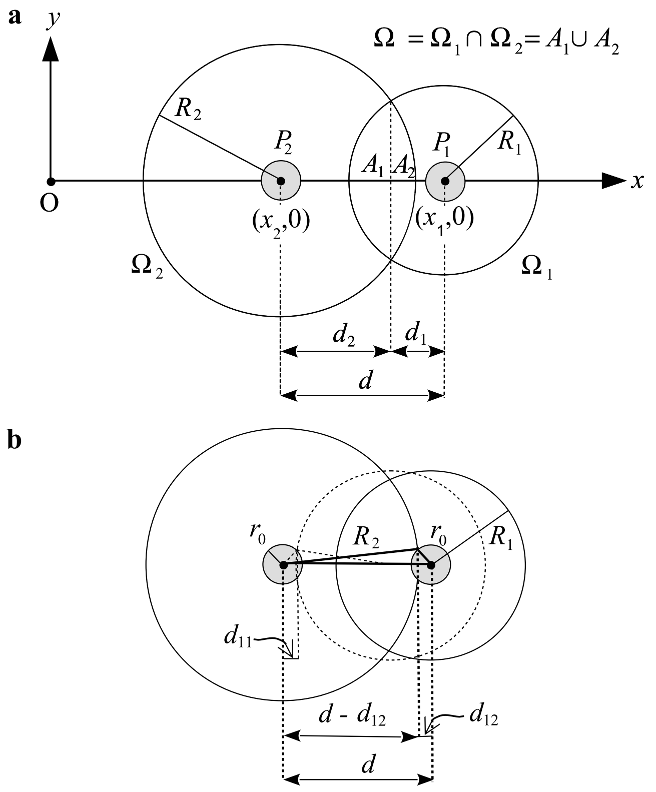

Fig. 6. A schematic diagram of the geometrical construction for the location of two defects P_1 and P_2 with centres of mass at positions $(x_1, 0)$ and $(x_2, 0)$, respectively, relative to a fixed origin **O** and at a separation distance d as shown. (a) The corresponding circular regions of influence, Ω_1 and Ω_2 with radii R_1 and R_2, respectively, as discussed in the text are displayed; their overlapping region is $\Omega = \Omega_1 \cap \Omega_2 = A_1 \cup A_2$ for the segments A_1 and A_2, as shown in the Figure. The distances d_1 and d_2 are introduced where $d = d_1 + d_2$. (b) The distances d_{11} and d_{12} are introduced for the calculations necessary in the evaluation of the interaction energy integrals as region Ω_1 overlaps Ω_2. The distance d_{12} arises as Ω_2 overlaps with the core defect in Ω_1. The dashed circle represents the situation when d reduces further as Ω_1 begins to overlap with the core defect in Ω_2, leading to the introduction of the distance d_{11}.

and, from the definition in Eq. (A.17),

$$\cos(\chi^1 - \chi^2) = \frac{1}{r_1 r_2}\left((x - x_1)(x - x_2) + y^2\right). \tag{7}$$

Since $x_2 = x_1 - d$, we can then write ω explicitly as

$$\begin{aligned}\omega = {} & \frac{I_1^2}{(x - x_1)^2 + y^2} + \frac{I_2^2}{(x - x_1 + d)^2 + y^2} \\ & + \frac{2I_1 I_2\left((x - x_1)(x - x_1 + d) + y^2\right)}{\left((x - x_1)^2 + y^2\right)\left((x - x_1 + d)^2 + y^2\right)}.\end{aligned} \tag{8}$$

We remark here that the third expression in Eq. (8) coincides with that discussed in [25, Eqn.(10.97)] in the special case when $x_1 = x_0$ and $x_2 = -x_0$ with $d = 2x_0 > 0$ and the region of integration was taken as an infinite strip in the xy-plane.

Before investigating examples in the next section we record here the integrations that will be carried out to evaluate the interaction energy which is crucial for the evaluation of the driving force $\mathbf{F}_1^{\text{int}}$ that will be introduced below. The integration limits will be given in terms of a rectangular Cartesian coordinate system so that they can be adapted for regions that are not necessarily circular, although a special case which has an exact integral for an annular region will be given in polar coordinates in Appendix C as an example that will be deployed in some evaluations. To simplify the integrations for a demonstration of the general techniques it will be assumed that $2R_1 + r_0 < R_2$, which is an assumption that will also fit with the example anaphase models proposed below for HeLa and C. elegans cells. This restriction allows us to consider the case when the region Ω_1 can be completely contained within Ω_2 with no overlap with the central core region in Ω_2. There is merit in considering this from the mathematical modelling perspective because this situation incorporates the possibility of obtaining an exact integral for the interaction energy when $R_1 + r_0 \leq d \leq R_2 - R_1$ which reveals its explicit behaviour and the consequent explicit force of interaction which can be used to compare the numerical derivations which have to be generally employed when Ω_1 is not necessarily completely embedded within Ω_2 or overlaps with the core region in Ω_2 (cf. for example, Eqs. (26), (27), Figs. 7, 9 and Appendix C). The restriction can of course be removed and the integrals calculated numerically, however, with this restriction, the energy in Eq. (4) is a function of d and can be written as

$$W(d) = \begin{cases} A_1(d) + A_2(d), & \text{if} \quad R_2 - R_1 \leq d \leq R_1 + R_2, \\ A_3(d), & \text{if} \quad 2r_0 \leq d < R_2 - R_1, \end{cases} \tag{9}$$

where, by symmetry in y and the notation introduced for the overlapping annular regions and segments described in Fig. 6,

$$A_1(d) = K\int_{d-\min\{R_1, d-d_{11}(d)\}}^{d-d_1(d)} \int_{L(x,d)}^{U_1(x,d)} \omega \, dy dx, \tag{10}$$

$$A_2(d) = K\int_{d-d_1(d)}^{\min\{R_2, d-d_{12}(d)\}} \int_{L(x,d)}^{U_2(x)} \omega \, dy dx, \tag{11}$$

$$A_3(d) = K\int_{d-\min\{R_1, d-d_{11}(d)\}}^{d+R_1} \int_{L(x,d)}^{U_1(x,d)} \omega \, dy dx, \tag{12}$$

and we have set

$$U_1(x,d) = \sqrt{R_1^2 - (x-d)^2}, \tag{13}$$

$$U_2(x) = \sqrt{R_2^2 - x^2}, \tag{14}$$

$$L(x,d) = \begin{cases} \sqrt{r_0^2 - x^2}, & \text{if} \quad |x| < r_0, \\ \sqrt{r_0^2 - (x-d)^2}, & \text{if} \quad |x - d| < r_0, \\ 0, & \text{otherwise}. \end{cases} \tag{15}$$

The integrals $A_1(d)$ and $A_2(d)$ are integrals over the area segments A_1 and A_2, respectively, as pictured in Fig. 6. The integral A_3 is evaluated whenever the region Ω_1 is contained entirely within the region Ω_2. If $2R_1 + r_0 \geq R_2$ then the integrals require modified integration limits; nevertheless, similar problems are tractable in such cases by adapting the methods presented here.

In Appendix B it is shown that the resulting internal force exerted by P_2 on P_1 is $\mathbf{F}_1^{\text{int}}$ and is given by, with $\hat{\mathbf{x}}$ set as the basis vector for the x-direction,

$$\mathbf{F}_1^{\text{int}} = -\frac{dW}{dd}\,\hat{\mathbf{x}}. \tag{16}$$

This follows the usual derivation of force as discussed in [26], [15, p. 427], and [3, p. 122]. We note from Appendix B that $\mathbf{F}_2^{\text{int}} = -\mathbf{F}_1^{\text{int}}$. In this problem, there will also be additional drag forces acting on the defects during their motion as they are attracted to each other, which can be written, respectively for P_1 and P_2, as

$$\mathbf{F}_1^{\text{ext}} = -\xi_1 \dot{\mathbf{r}}_1, \qquad \mathbf{F}_2^{\text{ext}} = -\xi_2 \dot{\mathbf{r}}_2, \tag{17}$$

where a superposed dot represents the derivative with respect to time and ξ_1 and ξ_2 are the corresponding coefficients with dimensions of mass divided by time.

This particular two-particle system can be transformed to a simplified system of two governing equations as outlined in Appendix B. The first is an equation for the motion of the centre of mass of the system located at $\mathbf{R}(t)$ defined by (B.3) in Appendix B as

$$\mathbf{R} = \frac{1}{m}\left(m_1 \mathbf{r}_1 + m_2 \mathbf{r}_2\right), \tag{18}$$

where we have set $m = m_1 + m_2$. The second is for the motion of a fictitious particle with position $\mathbf{r}(t) = \mathbf{r}_1 - \mathbf{r}_2$ and of reduced mass μ, defined in Eq. (22), under the influence of the internal force $\mathbf{F}^{\text{int}}$ (which turns out to be identical to that acting on P_1, namely, $\mathbf{F}_1^{\text{int}}$) and the external drag force $\mathbf{F}^{\text{ext}}$ acting on the particle of reduced mass. Under the approximating assumptions in Appendix B, the drag force acting on this fictitious particle is

$$\mathbf{F}^{\text{ext}} = -\xi\dot{\mathbf{r}}, \tag{19}$$

where ξ is the reduced coefficient defined in (22) below. Following the notation and details in Appendix B, the resulting equations from (B.12) and (B.13) are

$$\ddot{\mathbf{R}} = -\lambda_1\dot{\mathbf{R}}, \tag{20}$$

$$\mu\ddot{\mathbf{r}} = \mathbf{F}_1^{\text{int}} - \xi\dot{\mathbf{r}}, \tag{21}$$

where we write

$$\lambda_1 = \frac{\xi_1}{m_1}, \qquad \mu = \frac{m_1 m_2}{m}, \qquad \xi \equiv \frac{m_2}{m}\,\xi_1 = \frac{m_1}{m}\,\xi_2\,. \tag{22}$$

Eq. (21) is a version of Newton's second law of motion for a particle of reduced mass μ. A general review of drag forces experienced by nematic liquid crystal defects can be found in [15, §11.5].

In this approach to the problem it will be assumed that the initial velocities of the defects are each equal to zero, that is,

$$\dot{\mathbf{r}}_1 = \mathbf{0}, \quad \dot{\mathbf{r}}_2 = \mathbf{0}. \tag{23}$$

It then follows from the solution (B.14) in Appendix B to Eq. (20) that the centre of mass of the reduced system remains fixed at its original position $\mathbf{R}(0)$ given by

$$\mathbf{R}(0) = \frac{1}{m}\left(m_1\mathbf{r}_1(0) + m_2\mathbf{r}_2(0)\right), \tag{24}$$

and therefore it only remains to solve Eq. (21) for $\mathbf{r}(t)$ with prescribed initial conditions, where the initial locations of the defects are set at $\mathbf{r}_1(0)$ and $\mathbf{r}_2(0)$.

It sometimes proves convenient to work in polar coordinates centred at P_1 as in Appendix C relative to a fixed origin at $\mathbf{O}$ for the purposes of calculating the interaction energy explicitly, namely, $x = r\cos\theta + x_1$, $y = r\sin\theta$. From (C.2) and (C.3) it follows that

$$\omega = \frac{I_1^2}{r^2} + \frac{I_2^2}{r^2 + 2rd\cos\theta + d^2} + \frac{2I_1I_2(r + d\cos\theta)}{r(r^2 + 2rd\cos\theta + d^2)}\,. \tag{25}$$

For example, if $R_1 + r_0 \le r \le R_2 - R_1$ then region Ω_1 lies entirely within region Ω_2 and an exact integral is available for the energy $W(d)$ in Eq. (4) as derived in Appendix C, namely,

$$W(d) = \pi K I_1^2 \ln\left(\frac{R_1}{r_0}\right) - \frac{1}{2}K\pi I_2^2 \ln\left(\frac{d^2 - R_1^2}{d^2 - r_0^2}\right), \tag{26}$$

which gives the energy per unit depth in the z-direction. In all other cases it is more convenient to calculate the overlapping energies numerically. This result can also be used to verify the accuracy of the numerical evaluation of $W(d)$ for the relevant restricted range of d for which it is valid, as will be shown in Figs. 7(a),(c) and 9(a),(c). The integration limits in Eqs. (10) to (15) can also be adapted to other forms of regions of influence, for example rectangles or infinite strips in the plane. In this frame of reference the force F_1^{int} that arises between the two defects is therefore

$$F_1^{\text{int}} = -\frac{\mathrm{d}W}{\mathrm{d}d} = -K\pi I_2^2 \frac{d(R_1^2 - r_0^2)}{(R_1^2 - d^2)(d^2 - r_0^2)}, \tag{27}$$

which is clearly valid for $R_1 + r_0 \le d \le R_2 - R_1$. This force is positive, which indicates a repulsion between the two defects (cf. [3, p. 122]). This is not surprising given the overall forms of the energies for the examples investigated below in Figs. 7(a) and 9(a) where the exact interaction energy is displayed for physical parameters corresponding to the range of values for d discussed here; when I_1 and I_2 have opposite signs then the energy must rise as d decreases in order to achieve a sufficient energy level to initiate an attraction at which point the force changes sign and the defect with index I_1 is then attracted to the defect with index I_2 in the geometry of Fig. 6. This can occur as the overlap in the regions of influence increases with a consequent increase in energy until the defects are 'captured' at a critical distance d_c for an attractive interaction that initiates anaphase A. In anaphase the sizes of these regions are a proxy for the influence of the biochemical processes and for the examples explored below the critical distance in anaphase A will always be less than the values of d that are valid for the results available in Eqs. (26) and (27).

The aforementioned details are given for the two-body problem in anaphase A. They apply equally to the two-body problem in anaphase B with a simple change throughout of the suffixes 1 and 2 to 2 and 3, respectively. However, in anaphase B the indexes I_2 and I_3 have the same sign and so there is always a repulsion between the defects and, if desired, the exact derivation of the force in (27) can be deployed in calculations; we will not require to use it explicitly here for the basic ranges of d selected in the modelling for anaphase B, although the result will be of use for estimating the approximate magnitudes of the forces that are involved in the interactions.

5. Examples

We now explore two examples to demonstrate the model in relation to physical data: the HeLa cell and C. elegans. The energies in these examples have been evaluated using Eqs. (9) to (15) and the standard integration package available in Maple 2021 [27]. The final results have been prepared for presentation in the graphics package OriginPro 2021 [28].

5.1. HeLa cell

A typical length for a HeLa cell chromatid can be estimated as half of that for an average human chromosome of around 120 Mb (mega base pairs), and so we select a chromatid length of 60 Mb. Each base pair can be estimated as having a mass[2] of 650 Da $\approx 1.079 \times 10^{-9}$ pg and so the mass of a typical HeLa chromatid can be approximated as 6.47×10^{-2} pg, which can be set as m_1; this is in line with the chromosome masses reported in [29]. Such a chromatid can be identified as a $-1/2$ kinetochore defect located at P_1 (cf. Figs. 2 and 4).

An average microtubule is made up of around 1600 α/β-tubulin heterodimers per μm, with each heterodimer having a mass of around 100 kDa [1, p. 925] and therefore each microtubule has a mass of approximately 16×10^4 kDa per μm (cf. [30, pp. 64–65]). In the HeLa cell during anaphase A a microtubule has an average length of around 4 μm [31,32] which leads to a microtubule of mass 1.06×10^{-3} pg. However, this microtubule is connected in parallel to a large collection of nearby similar microtubules that form the kinetochore fibre (the bold lines in Fig. 2). We propose, for modelling purposes, that the MAP within the kinetochore fibre can be identified as a $+1/2$ defect (cf. Figs. 2, 4 and 5) that is located within this connected body of microtubules which form the kinetochore fibre with a combined mass of approximately 30 microtubules [12,33], and therefore we set $m_2 = 3.18 \times 10^{-2}$ pg and denote this combined body as MAP$^+$. The location P_2 is identified as the position of this $+1/2$ MAP defect within the kinetochore fibre which is then taken as the centre of its mass for modelling purposes. This location is selected as a modelling parameter which is set in the examples that follow; modifications to this position are possible and the general modelling procedure remains unchanged. The kinetochore fibre associated with each chromatid is therefore approximated at 4 μm in length with the MAP located near the fibre end that is closer to the kinetochore; the MAP location is set explicitly in the examples below.

---

[2] $1\,\text{Da} \doteqdot 1.660539066 \times 10^{-24}$ g.

The spindle pole (cf. Figs. 2 and 3) consists of two centrioles (a mother centriole and a daughter centriole) each made up of 27 microtubules and can be identified as a +1 defect (cf. Fig. 4) located at the position P_3. Each microtubule in the spindle pole has a length of approximately 0.5 μm and, from the previous calculations, a microtubule has a mass of 16×10^4 kDa per μm and so the spindle pole has a mass of 4.32×10^6 kDa which we can set as $m_3 = 7.17 \times 10^{-3}$ pg.

Anaphase occurs when the three bodies located at P_1, P_2 and P_3 mutually interact and is often observed as having a first interaction followed by a second interaction, labelled anaphase A and anaphase B, respectively [32], as mentioned above, and in this elementary approach will be treated as a pair of two-body problems under the presumption that there are distinct observations of anaphase B occurring directly after anaphase A, as observed in [31,34] for HeLa cells. The first, anaphase A, will model the attractive interaction between the $-1/2$ and $+1/2$ defects at positions P_1 and P_2, respectively. The second, anaphase B, will consider the repulsive interaction between the $+1/2$ and $+1$ defects at P_2 and P_3 where there will be a revised mass for the defect core located at P_2, due to it being attached to the $-1/2$ defect (chromatid) after the anaphase A interaction. The core radii of the three defects will be set equal to $r_0 = 0.1$ μm, as we again follow the illustration in Fig. 6. Note that each microtubule has a diameter of 24 nm (see Fig. 1) and so the end of the kinetochore fibre, which contains the ends of 30 microtubules in this model, may be accommodated on a kinetochore surface because the diameter of each core is assumed to be $2r_0 = 200$ nm. Anaphases A and B will be considered in turn and then the results will be combined for the model of the full anaphase. This model aligns with the summary information in the review article [32] for general timescales and data for anaphase A and anaphase B in human cells driven by force-generating mechanisms.

Anaphase A

It will be supposed that the region of influence for the $-1/2$ kinetochore defect at P_1 is smaller than that for the $+1/2$ MAP defect located at P_2 and choose to set $R_1 = 5$ μm and $R_2 = 11$ μm and that the core radii of the two defects are set equal to $r_0 = 0.1$ μm, as illustrated in Fig. 6. During anaphase A it is assumed that the spindle pole at P_3 can be modelled as stationary. It is the MAP within the microtubule that is crucial in the anaphase A process as it evolves, which is why it is the focus of the dynamics via its position at P_2. Accordingly, we can set, in the notation of Fig. 6,

$$\mathbf{r}_1(t) = (x_1(t), 0), \qquad \mathbf{r}_2(t) = (x_2(t), 0), \tag{28}$$

$$\mathbf{r}(t) = \mathbf{r}_1(t) - \mathbf{r}_2(t) = (d(t), 0), \tag{29}$$

where

$$d(t) = x_1(t) - x_2(t). \tag{30}$$

The fixed centre of mass for the reduced system is given by (24). The resulting dynamic equation in this geometry for the interaction of the defects is then, from (19) and (21),

$$\mu \ddot{d} = F_1^{\rm int} - \xi \dot{d}. \tag{31}$$

The force of interaction as defined in Eq. (16) is a function of d given by

$$F_1^{\rm int} = -\frac{{\rm d}W}{{\rm d}d}, \tag{32}$$

and the initial conditions for the differential equation in $d(t)$ are

$$\dot{d}(0) = 0, \quad d(0) = x_1(0) - x_2(0), \tag{33}$$

due to the assumption (23) that the initial velocities can be set to zero in a first investigation, which means that the centre of mass $\mathbf{R}(t)$ of the reduced system remains fixed at $\mathbf{R}(0)$ given by (24). From the notation in Eqs. (28) to (30) and the results from Eqs. (B.15) and (B.16) in Appendix B it is seen that the solutions for $x_1(t)$ and $x_2(t)$ are given by

$$x_1(t) = R(0) + \frac{m_2}{m} d(t), \tag{34}$$

$$x_2(t) = R(0) - \frac{m_1}{m} d(t), \tag{35}$$

where, from Eq. (24), the initial position for the reduced system, $R(0)$, is given by

$$R(0) = \frac{1}{m}\left(m_1 x_1(0) + m_2 x_2(0)\right). \tag{36}$$

Further, from Eqs. (34), (35) and the definitions of ξ_1 and ξ_2 in Eq. (22), the drag forces acting on each defect satisfy the equalities

$$-\xi \dot{d}(t) = -\xi_1 \dot{x}_1(t) = \xi_2 \dot{x}_2(t). \tag{37}$$

There are obvious analogues to Eqs. (28) to (37) for the two-body problem in terms of the defects located at P_2 and P_3. Consequently, the magnitude of the average drag force, denoted by $\widehat{F}^{\rm d}_A$, is given by

$$\widehat{F}^{\rm d}_A \equiv \frac{\xi}{t_A}\left|\int_0^{t_A} \dot{d}(s)\, ds\right| = \frac{\xi}{t_A}\left|d(t_A) - d(0)\right|, \tag{38}$$

where t_A is the corresponding timescale for anaphase A (similarly for the average drag force $\widehat{F}^{\rm d}_B$ for anaphase B in terms of t_B).

The elastic constant in the Dafermos interaction energy (4) can be approximated as $K = 5$ pN [5] from data known for anisotropic materials. The corresponding energy $W(d)$, in picojoules (pJ), for the given regions of influence and parameters listed in Table 1 is shown in Fig. 7(a). This energy is valid for 0.2 μm $= 2r_0 \le d \le R_1 + R_2 = 16$ μm. The numerically derived energy is plotted over this entire available range of d using the results in Eqs. (9) to (15) and standard integration available in Maple 2021 while the exact energy has been plotted using Eq. (26) over the restricted range of d for which it is valid, namely, $R_1 + r_0 \le r \le R_2 - R_1$. Since W represents the energy per unit depth in the z-direction, the calculated energy has additionally been multiplied by a typical depth commensurate with the scale of the smaller regions of influence, set throughout the examples in this section at 2 μm. Other depths can be chosen and the model will remain valid within the constraints of a two-dimensional description although it is anticipated that depths beyond the scale of the regions of influence would really require a revised three-dimensional model, which is beyond the scope of this present work. This selected depth can enable meaningful comparisons with data in the literature, for example when calculating forces. As mentioned after Eq. (27), the consequent force of interaction becomes attractive only when d is at a suitably close distance less than the critical distance d_c where the force changes sign, as can be deduced from Fig. 7(a) and the definition of the force $F_1^{\rm int}$ in Eq. (32). In this example, $d_c \doteqdot 4.14$ μm and we therefore choose to set the initial data, for illustrative purposes that will become clear below, as

$$x_1(0) = 14 \ \mu\text{m}, \quad x_2(0) = 10 \ \mu\text{m}, \quad \dot{x}_1(0) = 0, \quad \dot{x}_2(0) = 0, \tag{39}$$

which leads to the initial conditions

$$d(0) = 4 \ \mu\text{m}, \quad \dot{d}(0) = 0. \tag{40}$$

The solution $d(t)$ to the dynamic equation (31) with initial conditions (40) can then be determined numerically using the dsolve package within Maple 2021, noting that the reduced mass for anaphase A in this problem is, by the definition in (22), $\mu = 2.13 \times 10^{-2}$ pg. The only unknown that is required to obtain a solution is the value of the reduced coefficient ξ. This can be estimated by knowing the duration times that are observed from experiments for anaphases A and B. From the data in [34] it is know that for many HeLa cells the timescales for both anaphase A and anaphase B are very similar at around 3 min for each in observations. This leads, in these experiments, to a total anaphase timescale of around 6 min. This timescale is determined by ξ and, by numerical investigations for differing values of ξ, a solution can be obtained that leads to such a timescale for anaphase A. We choose to set ξ_A as the calculated value that leads to the timescale of $t_A = 180$ s for the duration of anaphase A where, given the core size of the defects,

Table 1
Approximate material parameters and their values. They have been derived from the experimental observations cited in the text: principally from [31,32,34] for the HeLa cell and [35–39] for C. elegans. The MAP$^+$ mass for anaphase B, m_{22}, has been set equal to $m_1 + m_2$.

Parameter	Symbol	HeLa	C. elegans
Elastic constant	K	5 pN	5 pN
Core radius	r_0	0.1 μm	0.1 μm
Chromatid defect	I_1	$-\frac{1}{2}$	$-\frac{1}{2}$
MAP$^+$ defect	I_2	$+\frac{1}{2}$	$+\frac{1}{2}$
Spindle pole defect	I_3	$+1$	$+1$
Chromatid region of influence	R_1	5 μm	2.5 μm
MAP$^+$ region of influence (anaphase A)	R_2	11 μm	6 μm
MAP$^+$ region of influence (anaphase B)	R_{22}	1 μm	1 μm
Spindle pole region of influence	R_3	5 μm	5 μm
Chromatid mass	m_1	6.47×10^{-2} pg	8.25×10^{-3} pg
MAP$^+$ mass (anaphase A)	m_2	3.18×10^{-2} pg	1.06×10^{-2} pg
MAP$^+$ mass (anaphase B)	m_{22}	9.65×10^{-2} pg	1.89×10^{-2} pg
Spindle pole mass	m_3	7.17×10^{-3} pg	7.17×10^{-3} pg

Table 2
Numerical modelling parameters for a HeLa cell. The coefficients ξ_A and ξ_B are the basic numerical modelling parameters and are selected to achieve the typical physical timescales reported in [34]. The material parameters used in numerical calculations are those listed in Table 1.

Parameter	Symbol	Value
HeLa cell		Anaphase A
Reduced mass	μ	2.13×10^{-2} pg
Reduced coefficient	ξ_A	2.61×10^{-1} g s^{-1}
Effective coefficient for chromatid	ξ_{A_1}	7.91×10^{-1} g s^{-1}
Effective coefficient for MAP$^+$	ξ_{A_2}	3.89×10^{-1} g s^{-1}
Anaphase A duration time	t_A	180 s
magnitude of average drag force	$\widehat{F}_A^{\mathrm{d}}$	5.51 pN
HeLa cell		Anaphase B
Reduced mass	μ	6.67×10^{-3} pg
Reduced coefficient	ξ_B	9.14×10^{-1} g s^{-1}
Effective coefficient for MAP$^+$	ξ_{B_2}	13.21 g s^{-1}
Effective coefficient for spindle pole	ξ_{B_3}	9.81×10^{-1} g s^{-1}
Anaphase B duration time	t_B	180 s
magnitude of average drag force	$\widehat{F}_B^{\mathrm{d}}$	20.31 pN

$d(t_A) = 2r_0$ when the two cores meet. In this particular example, it was determined that

$$\xi_A = 2.61 \times 10^{-1}\ \mathrm{g\ s}^{-1}, \quad t_A = 180\,\mathrm{s}, \tag{41}$$

with corresponding coefficients given via (22) and consequently, in an obvious notation corresponding to the solutions for $x_1(t)$ and $x_2(t)$,

$$\xi_{A_1} = 7.91 \times 10^{-1}\ \mathrm{g\ s}^{-1}, \quad \xi_{A_2} = 3.89 \times 10^{-1}\ \mathrm{g\ s}^{-1}. \tag{42}$$

Moreover, the magnitude of the average drag force defined by Eq. (38) is

$$\widehat{F}_A^{\mathrm{d}} = 5.51\,\mathrm{pN}. \tag{43}$$

A summary of the modelling parameters is given in Table 2 and the solution for $d(t)$ is shown in Fig. 7(b). The final solutions for $x_1(t)$ and $x_2(t)$ are recovered via $d(t)$ and the relations in Eqs. (34), (35), (36) and (39) and these are displayed in Fig. 8(a).

The point $x_2^+(0)$ is defined to be the initial position in anaphase B of the combined MAP$^+$ and chromatid which is set to be the point of contact of the two cores in anaphase A which is given by

$$x_2^+(0) = \frac{1}{2}\left(x_1(t_A) + x_2(t_A)\right). \tag{44}$$

The constant value assumed for the spindle pole throughout anaphase A is set to be the initial point $x_3(0)$ in anaphase B, which is given by

$$x_3(0) = x_2^+(0) - d(0), \tag{45}$$

with $d(0)$ set at an appropriate value for anaphase B that will be given below in Eq. (48).

Anaphase B

To model anaphase B as a two-body problem we assume that the chromatid and the microtubule with its link to MAP$^+$ form one body and that this combined $+1/2$ defect, with position denoted by $x_2^+(t)$, then interacts with the spindle pole, which is modelled as a $+1$ defect. We therefore introduce a revised mass for the combination of the MAP$^+$ and chromatid and set it as $m_{22} = m_1 + m_2$. We can follow the procedures used in anaphase A and again use the geometry in Fig. 6 with the positions of x_2 and x_1 replaced, respectively, by x_3 and x_2^+, with I_2 replaced by I_3 and I_1 replaced by I_2 accordingly. We also choose to set a revised radius for the region of influence around the $+1/2$ defect as $R_{22} = 1$ μm and set $R_3 = 5$ μm, with the distance between the two defects being $d(t) = x_2^+(t) - x_3(t)$. The interaction energy density in (25) and interaction energy W in (4) can be adapted accordingly, as can Eqs. (28) to (33). The numerically derived energy is plotted in Fig. 7(c) for the data listed in Table 1 over the interactive range 1.1 μm $= R_{22} + r_0 \le d \le R_{22} + R_3 = 6$ μm, with the exact energy plotted over its entire domain of validity $R_{22} + r_0 \le d \le R_3 - R_{22}$.

The governing differential equation and force of interaction are given in this case by Eqs. (31) and (32) where W is replaced by the energy for anaphase B. It is clear from Fig. 7(c) that the force F_1^{int} is always positive and that these defects of the same sign therefore always repel in anaphase B, as mentioned previously. The calculations in anaphase B are similar to those in anaphase A with given initial positions for $x_2^+(0)$ and $x_3(0)$, evaluated by suitably adapting the results in (9) to (15) in the context of the data for anaphase B. We choose to set the initial conditions as

$$x_2^+(0) = \frac{1}{2}\left(x_1(t_A) + x_2(t_A)\right), \; x_3(0) = x_2^+(0) - d(0), \tag{46}$$

$$\dot{x}_2^+(0) = 0, \; \dot{x}_3(0) = 0, \tag{47}$$

with $d(0) = R_3 - R_{22}$ in this case, chosen so that the displacement of the spindle pole in anaphase B approximates that observed in the experimental data of [34]. Note that the overlap for the interactive energy ceases when $d > R_{22} + R_3$. The initial conditions for Eq. (31) are therefore

$$d(0) = R_3 - R_{22} = 4\ \mu\mathrm{m}, \quad \dot{d}(0) = 0. \tag{48}$$

The region of influence Ω_2 around x_2 initially lies completely inside the region of influence Ω_3 around x_3, and so the initial overlap area is completely within the Ω_3 region. The reduced mass for anaphase B is, by the definition (22) in terms of m_{22} and m_3, $\mu = 6.47 \times 10^{-3}$ pg. Similarly, we set ξ_B to be the calculated value that leads to the timescale of t_B for the same duration of anaphase A, that is, 3 min and note that in this case $d(t_B) = R_{22} + R_3$. It was determined that

$$\xi_B = 9.14 \times 10^{-1}\ \mathrm{g\ s}^{-1}, \quad t_B = 180\,\mathrm{s}, \tag{49}$$

with corresponding coefficients given via (22) to find that

$$\xi_{B_2} = 13.21 \times \mathrm{g\ s}^{-1}, \quad \xi_{B_3} = 9.81 \times 10^{-1}\ \mathrm{g\ s}^{-1}. \tag{50}$$

The magnitude of the average drag force is, by the analogue of Eq. (38),

$$\widehat{F}_B^{\mathrm{d}} = 20.31\,\mathrm{pN}. \tag{51}$$

The solution to Eq. (31) for $d(t)$ in terms of the energy for anaphase B is shown in Fig. 7(d) and a summary of the parameters is presented in Table 2. The solutions displayed in Fig. 8(a) have been determined from $d(t)$ via the analogues of Eqs. (34) to (36) and the initial conditions (46) and are labelled as $x_2^+(t)$ and $x_3(t)$. Recall that the plus index indicates

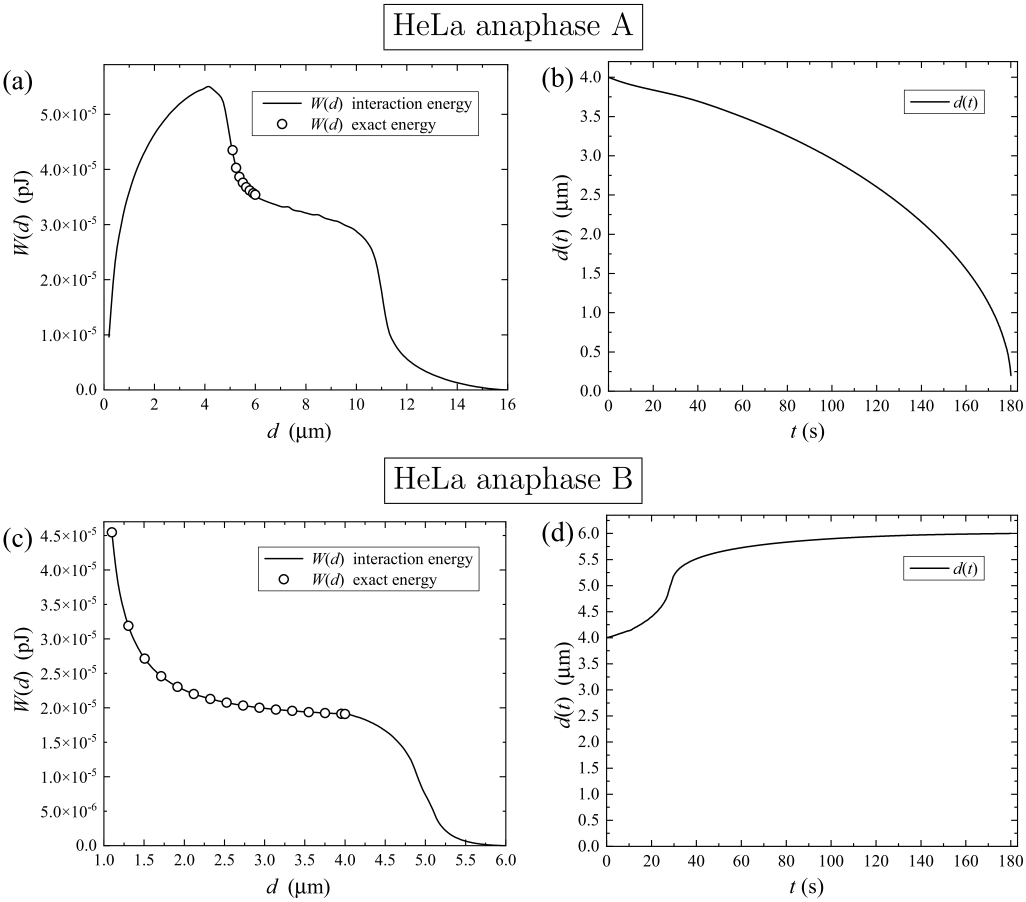

Fig. 7. (a) The interaction energy for the chromatid ($I_1 = -1/2$) and the MAP$^+$ ($I_2 = +1/2$) as a function of the distance d between these two defects in the model of anaphase A discussed in the text. (b) The solution $d(t)$ of the governing dynamic Eq. (31) for anaphase A for the energy shown in (a) for the initial conditions (40). (c) The interaction energy for the MAP$^+$ and the spindle pole ($I_3 = +1$) as a function of the distance d between them in the model for anaphase B. (d) The solution $d(t)$ of the governing Eq. (31) for anaphase B for the energy shown in (c) for the initial conditions (48). In both (a) and (c) the bold curves have been calculated numerically and the circles are points calculated from the exact energy formula given in (26) over the domain for which it is valid, details in the text.

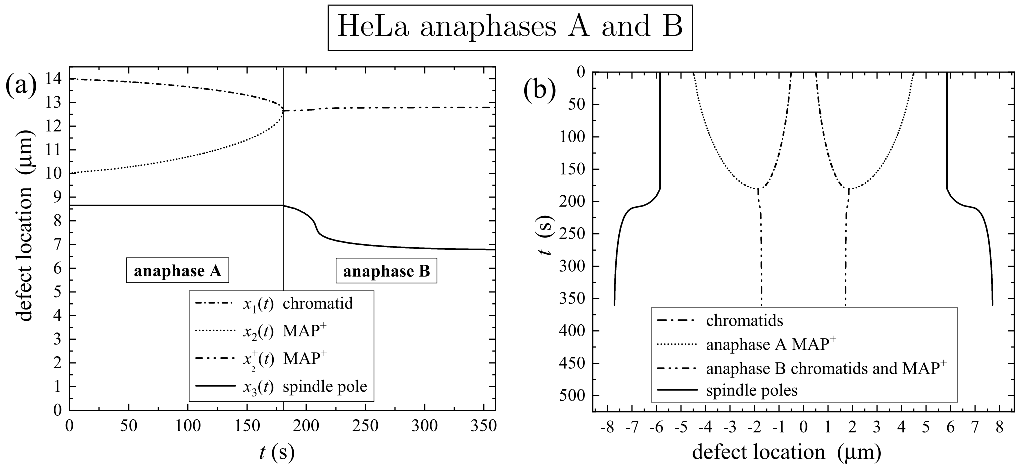

Fig. 8. Anaphase for a HeLa cell obtained from calculations based on the material parameters in Table 1 and the reduced coefficients ξ_A and ξ_B as key modelling parameters given in Table 2. The timescales presented here are in line with the experimental times reported in [34]. (a) Anaphase A is modelled first as a two-body problem for the chromatid and the MAP$^+$ being attracted while the spindle pole is presumed fixed. Anaphase A has a duration of $t_A = 180\,\mathrm{s}$. Anaphase B follows the cessation of anaphase A as the MAP$^+$ and the spindle pole repel each other; it is assumed that the MAP$^+$ and chromatid move together as one joined body for the duration of anaphase B with a duration of $t_B = 180\,\mathrm{s}$ which then leads to a total duration time of 360 s for anaphase A followed by anaphase B. (b) A kymograph obtained by the method outlined in the text of the chromatids and spindle poles relative to the original cell central mid-plane which can be used to compare with the kymograph data available, for example, in [31].

that the path modelled is that of the combined chromatid and MAP$^+$ which means that the solution for the chromatid, $x_1(t)$, is presumed to coincide with $x_2^+(t)$ during anaphase B. There is also an obvious linear time shift for the anaphase B solutions for display purposes with the initial and final times set to 180 s and 360 s, respectively.

The final solutions for anaphases A and B are shown in Fig. 8(a); the corresponding kymograph is in Fig. 8(b) which can more readily be compared to those obtained from experimental studies of HeLa cells in the literature, for example those available in [31]. The kymograph is obtained from the solutions in Fig. 8(a) by linearly translating the initial data to the locations shown in Fig. 8(b) with the centre of the cell located at $x = 0$, supplemented by the right half of the cell behaviour which occurs simultaneously and is assumed to be identical to that obtained for the left half with, of course, movement in the opposite direction. The kymograph reflects the time-dependent evolution of anaphase and is effectively tracking the movement of the centrioles, kinetochores and chromatids: Fig. 2 is a schematic example of one snapshot in time of their locations in the kymograph.

Some discussion of drag forces in mitosis has been made in [40]. These authors modelled a chromosome as a cylinder and their initial estimate for the coefficient in the drag force is $\xi \approx 5.5 \times 10^{-2}$ g s^{-1} which resulted in an estimate for the drag force of $F^{\mathrm{d}} \approx 0.9$ pN when the speed of the chromosome was estimated at 16 nm s^{-1}. In the HeLa example presented here for the motion of the chromatid in anaphase A, represented as the defect with index $I_1 = -1/2$, the coefficient in the drag force was found to be $\xi_A = 2.61 \times 10^{-1}$ g s^{-1}, the average drag force was $F_A^{\mathrm{d}} = 5.51$ pN and the average speed of the chromatid was approximately 7 nm s^{-1}. Although not used directly to derive the solutions in this HeLa example because the validity of its range was outside the relevant applicable data used here, it is worth noting that the magnitude of the average of the force given explicitly by Eq. (27) can be evaluated for the HeLa data in Table 1 to find $\widehat{F}_1^{\mathrm{int}} = 9.00$ pN in anaphase A and $\widehat{F}_1^{\mathrm{int}} = 9.09$ pN in anaphase B. The results presented here are generally within an order of magnitude of those estimated in [40] and there is clearly more that can be explored by varying the material parameters and regions of influence in our model.

5.2. *C. elegans*

An average C. elegans chromatid can be identified as a $-1/2$ kinetochore defect located at P_1 and its mass needs to be determined. From the experimental results in [39] it is known that a C. elegans haploid genome is expected to contain 8×10^7 base pairs with a mass of 8.8×10^{-14} g. This results in each base pair having a mass of approximately 1.1×10^{-21} g. From the results reviewed in [38] an average chromosome in C. elegans consists of approximately 15 Mb (mega base pairs) and so a chromatid can be estimated as having 7.5 Mb which equates to a mass of 8.25×10^{-3} pg, which can be set as m_1.

In C. elegans the microtubule has a length of around 5 μm when anaphase A begins [37, Fig. 4]. By similar calculations to those described above for the HeLa cell, this gives a mass of 8×10^5 kDa which is approximately 1.33×10^{-3} pg for a single microtubule. However, it is known [35] that the kinetochore fibres for C. elegans each consist of around 8 microtubules and therefore, for reasons similar to those for the HeLa example, we can be set $m_2 = 1.06 \times 10^{-2}$ pg. As before, the MAP will be contained within this kinetochore fibre. The MAP defect including the kinetochore fibre is again denoted by MAP$^+$.

The separation between anaphase A and anaphase B in C. elegans is often difficult to detect. For example, [36] do not detect anaphase A in C. elegans and [37] report that the duration of anaphase A is relatively short. Nevertheless, in this basic investigation it will be assumed that anaphase B occurs after anaphase A and we will be motivated by the data presented in Fig. 4 in [37] which displays a sequence of events, each occurring over time intervals of around 70 s. To accomplish this we again consider a pair of two-body problems and model anaphases A and B separately. However, as the key modelling parameters for the timescales are directly linked to the corresponding reduced coefficients ξ_A and ξ_B, we choose to set these values by numerical experimentation so that the timescale for the duration of anaphases A and B are both 70 s; if required, the same technique can be used to produce a shorter timescale for anaphase A by determining numerically an appropriate corresponding value for ξ_A.

Anaphase A

We set the core radii of the two defects to be equal to $r_0 = 0.1$ μm, as previously set for the HeLa cell example. It will be supposed that the region of influence for the $-1/2$ kinetochore defect at P_1 is smaller than that for the $+1/2$ MAP defect located at P_2 and choose in this example to set $R_1 = 2.5$ μm and $R_2 = 6$ μm. As before, during anaphase A the spindle pole at P_3 can be modelled as stationary. We adopt the notation and formulation in Eqs. (28) to (33) and assume that the initial velocities of the defects are zero as proposed in (23). The consequent energy $W(d)$ has been calculated via Eqs. (9) to (15) and multiplied by a typical depth of 2 μm to enable data comparisons, as previously carried out for the HeLa cell example. The result for the data prescribed in Table 1 is presented in Fig. 9(a), which also includes a plot of the exact energy for its available range $R_1 + r_0 \le d \le R_2 - R_1$. Analogous to the previous example, the consequent force of interaction in this instance becomes attractive only if d is less than the critical distance $d_c \doteqdot 2.05$ μm where the force changes sign and therefore we can choose the initial data for this C. elegans example for illustrative purposes to be

$$x_1(0) = 14\ \mu\text{m}, \quad x_2(0) = 12\ \mu\text{m}, \quad \dot{x}_1(0) = 0, \quad \dot{x}_2(0) = 0, \tag{52}$$

which leads to the initial conditions

$$d(0) = 2\ \mu\text{m}, \quad \dot{d}(0) = 0. \tag{53}$$

The relevant reduced mass for anaphase A is, by the definition in (22), $\mu = 4.65 \times 10^{-2}$ pg. Eq. (31) subject to the initial conditions (53) is solved numerically to obtain $d(t)$. As previously, the solution requires the identification of a suitable reduced coefficient ξ for this problem by exploring data from experiments and making comparisons with the numerically derived solutions. For the data presented above, and summarised in Table 1, the duration of anaphase A, t_A, was set to 70 s, which is when the two cores make contact and $d(t_A) = 2r_0$. It was determined that

$$\xi_A = 3.26 \times 10^{-1}\ \text{g s}^{-1}, \quad t_A = 70\,\text{s}, \tag{54}$$

and the other relevant coefficients determined via (22) as

$$\xi_{A_1} = 5.79 \times 10^{-1}\ \text{g s}^{-1}, \quad \xi_{A_2} = 7.74 \times 10^{-1}\ \text{g s}^{-2}. \tag{55}$$

The magnitude of the average drag force, from Eq. (38), is

$$\widehat{F}_A^{\mathrm{d}} = 8.38\,\text{pN}. \tag{56}$$

These results for anaphase A are summarised in Table 3. The solution for $d(t)$ is shown in Fig. 9(b) and the solutions for $x_1(t)$ and $x_2(t)$, which are recovered from $d(t)$ via Eqs. (34) to (36) and the initial data (52), are displayed in Fig. 10(a).

As in the HeLa example, we can define, in terms of the solutions for anaphase A for C. elegans, the initial position of the combined MAP$^+$ and chromatid in anaphase B as $x_2^+(0)$ given by Eq. (44) and the constant position assumed for the spindle pole throughout anaphase A can be set as $x_3(0) = x_2^+(0) - d(0)$, as defined in Eq. (45), with $d(0)$ to be set at an appropriate value for anaphase B, as discussed below.

Anaphase B

To model anaphase B we assume, as for the HeLa cell, that the chromatid and the microtubule form one body that constitutes the $+1/2$ defect with position $x_2^+(t)$ which then interacts with the $+1$ spindle pole defect located at $x_3(t)$. A revised mass for the combination of the MAP$^+$ and chromatid is introduced as $m_{22} = m_1 + m_2$. The mass of the spindle pole is taken to be the same as in the HeLa cell given above and so

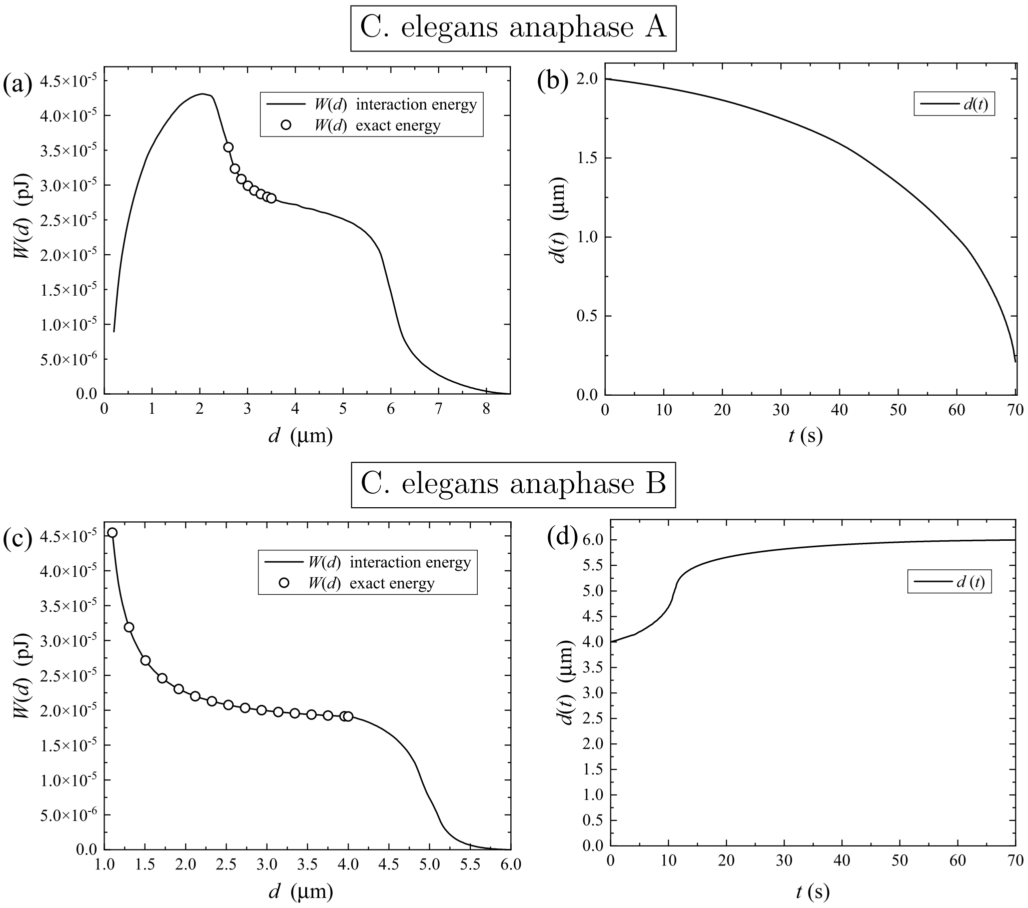

Fig. 9. (a) The interaction energy for the chromatid ($I_1 = -1/2$) and the MAP$^+$ ($I_2 = +1/2$) as a function of the distance d between these two defects in the model of anaphase A discussed in the text for C. elegans. (b) The solution $d(t)$ of the governing dynamic Eq. (31) for anaphase A for the energy shown in (a) for the initial conditions (53). (c) The interaction energy for the MAP$^+$ and the spindle pole ($I_3 = +1$) as a function of the distance d between them in the model for anaphase B. (d) The solution $d(t)$ of the governing Eq. (31) for anaphase B for the energy shown in (c) for the initial conditions (48). The bold curves in (a) and (c) were calculated numerically and the circles are points evaluated from the exact energy in (26) over its range of validity.

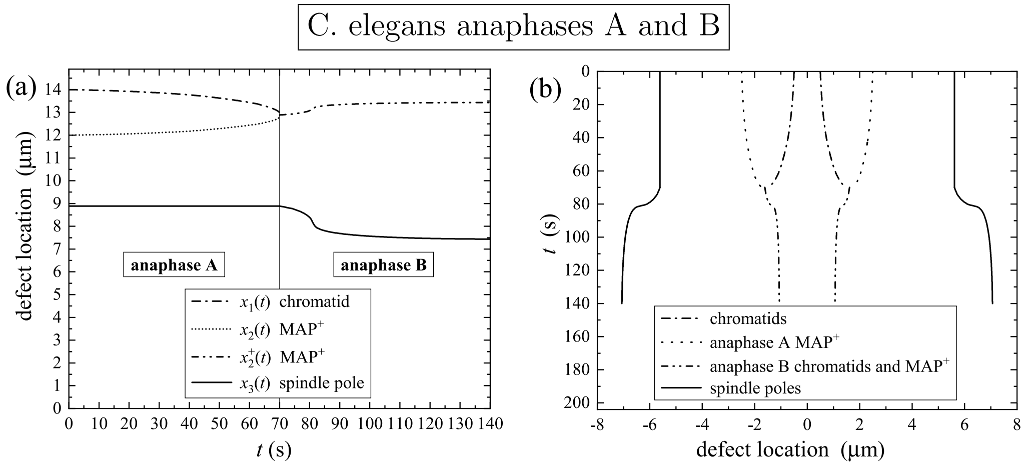

Fig. 10. Anaphase for a C. elegans cell. Calculations are based on the material parameters in Table 1 and the reduced coefficients ξ_A and ξ_B as key modelling parameters given in Table 3. (a) Anaphase A is modelled as a two-body problem for the chromatid and the MAP$^+$ being attracted while the spindle pole is presumed fixed. Anaphase A has a presumed duration of $t_A = 70$ s which determines the value of ξ_A. Anaphase B is presumed to occur after anaphase A, as discussed in the text, with a time duration $t_B = 70$ s, which determines ξ_B. These timescales are in line with the experimental times reported in [36,37]. (b) Kymograph of the chromatids and spindle poles relative to the original cell central mid-plane which can be used to compare with the kymograph data available in [36] and the experimental observations made in [37].

$m_3 = 7.17 \times 10^{-3}$ pg. The reduced mass for anaphase B is then, by the analogous definition in (22) in terms of m_{22} and m_3, $\mu = 5.20 \times 10^{-2}$ pg.

The procedures used in anaphase A can be used again in the geometry of Fig. 6 with the positions x_2 and x_1 replaced, respectively, by x_3 and x_2^+ and with I_2 replaced by I_3 and I_1 replaced by I_2. The interaction energy density contribution ω in (25) and interaction energy $W(d)$ in Eqs. (4) and (28) to (33) can then be adapted accordingly. In this instance we select $R_{22} = 1$ µm, $R_3 = 5$ µm and, for the purposes

Table 3

Numerical modelling parameters for C. elegans. The coefficients ξ_A and ξ_B are the basic numerical modelling parameters and are selected to achieve the typical physical timescales reported in [37] and [36]. The material parameters used in numerical calculations are those listed in Table 1.

Parameter	Symbol	Value
C. elegans		Anaphase A
Reduced mass	μ	4.65×10^{-3} pg
Reduced coefficient	ξ_A	3.26×10^{-1} g s^{-1}
Effective coefficient for chromatid	ξ_{A_1}	5.79×10^{-1} g s^{-1}
Effective coefficient for MAP$^+$	ξ_{A_2}	7.47×10^{-1} g s^{-1}
Anaphase A duration time	t_A	70 s
magnitude of average drag force	$\widehat{F}^{\mathrm{d}}_A$	8.38 pN.
C. elegans		Anaphase B
Reduced mass	μ	5.20×10^{-3} pg
Reduced coefficient	ξ_B	7.10×10^{-2} g s^{-1}
Effective coefficient for MAP$^+$	ξ_{B_2}	2.58×10^{-1} g s^{-1}
Effective coefficient for spindle pole	ξ_{B_3}	9.79×10^{-2} g s^{-1}
Anaphase B duration time	t_B	70 s
Magnitude of average drag force	$\widehat{F}^{\mathrm{d}}_B$	4.06 pN.

of modelling the interaction energy and the dynamics of the distance $d(t)$ between $x_2^+(t)$ and $x_3(t)$, set the initial conditions to be those set at Eqs. (46) and (47), but in the context of this example. The dynamic equation to be solved for $d(t)$ is then Eq. (31) with the initial conditions (48), observing that in this example $d(0) = R_3 - R_{22}$ also equals 4 μm. Note, as before, that the revised region of influence Ω_2 has radius $R_{22} = 1$ μm around x_2^+ so that initially it lies completely inside the region of influence Ω_3 centred at x_3. The energy $W(d)$ for the data prescribed in Table 1 is presented in Fig. 9(c), which also includes a plot of the exact energy available for the range $R_{22} + r_0 \leq d \leq R_3 - R_{22}$.

Eq. (31), with F_1^{int} given by (32) in terms of the energy $W(d)$ for anaphase B, subject to the initial conditions (48) can be solved numerically to obtain $d(t)$, which leads to the final solutions for $x_2^+(t)$ and $x_3(t)$ recovered from $d(t)$ via the obvious analogues of Eqs. (34) to (36) with initial data (46) in the context of anaphase B in this example. To ensure that $t_B = 70$ s, noting that $d(t_B) = R_{22} + R_3$, it was found that

$$\xi_B = 7.10 \times 10^{-2}\ \mathrm{g\ s^{-1}}, \quad t_B = 70\,\mathrm{s}, \tag{57}$$

with the other relevant coefficients determined from (22) as

$$\xi_{B_2} = 2.58 \times 10^{-1}\ \mathrm{g\ s^{-1}}, \quad \xi_{B_3} = 9.79 \times 10^{-2}\ \mathrm{g\ s^{-1}}. \tag{58}$$

The magnitude of the average drag force is, from Eq. (38),

$$\widehat{F}^{\mathrm{d}}_B = 4.06\,\mathrm{pN}. \tag{59}$$

These results are summarised for anaphase B in Table 3. The solution for $d(t)$ is shown in Fig. 9(d) and the solutions for $x_2^+(t)$ and $x_3(t)$ are displayed in Fig. 10(a). Similar to the HeLa cell example, $x_2^+(t)$ is the path for the combined chromatid and MAP$^+$ and the solution for the chromatid, $x_1(t)$, is presumed to coincide with $x_2^+(t)$ during anaphase B. A linear time shift for the anaphase B solutions has also been made for display purposes with the initial and final times set to 70 s and 140 s, respectively.

The final solutions for anaphases A and B are also shown in Fig. 10(b) in the corresponding kymograph obtained by the method outlined above for the HeLa cell. This can be compared to those available in the experimental literature, for example in the sequence of picture frames from *in vivo* live imaging for C. elegans in Fig. 4A in [37]; see also the kymograph results reported in [36].

6. Conclusions and future directions

In this paper anaphase in the mitosis of cells has been modelled in terms of liquid crystals. In particular, fundamental elements such as microtubules are modelled as flux lines of liquid crystal alignments which also model the various proteins associated with the key phases of cell mitosis. Anaphase A and anaphase B have been investigated based on the theory developed by Frank [24] and Oseen [41] combined with the interaction energy considerations of Dafermos [23]. Our theory has been exploited in application to HeLa and C. elegans cells and agrees well with the cited experimental results.

A more detailed study of the regions of influence introduced here is reserved for future investigations. Nevertheless, it is natural at this point to make one small observation. Each mitotic spindle pole can be modelled as a +1 defect as shown in Figs. 4 and 5 with an aster at its centre. If $(r_i, \chi^i), i = 1, 2$ denotes the position of each mitotic spindle as described in Appendix A, with overlapping regions of influence, then the contribution ω towards the energy density is given by Eq. (A.18) as

$$\omega = \frac{1}{{r_1}^2} + \frac{1}{{r_2}^2} + \frac{2}{r_1 r_2}\cos(\chi^1 - \chi^2). \tag{60}$$

It is known that defects of the same sign repel. Clearly, this energy is minimised when $\chi^1 - \chi^2 = \pi$ and $r_1 = r_2$, which is precisely the bipolar mitotic spindle observed and displayed in Fig. 2. Furthermore, the minimum energy is zero and is attained along the equatorial line bisecting the bipolar mitotic spindle axis. In [10,42,43] the dynamics of centriole movement is considered from the point of view of **Q**-tensor theory. The approach adopted here, which is based on the classical Frank–Oseen energy model [24,41] and the subsequent development by Dafermos in [23], therefore appears as an alternative direct way for identifying the equilibrium locations of the spindle poles as part of the mitotic spindle.

Recall that the sister chromatids separate during anaphase and move to opposite polar regions of the mitotic spindle. This process is distinguished by the two temporal events of anaphase A and anaphase B. Anaphase A modelled in terms of the two-body energy (A.18) is marked by the abrupt and synchronous separation of sister chromatids due to the sudden degradation of cohesion complexes between sister chromatids. Daughter chromosomes move to opposite spindle polar regions as their kinetochore fibres shorten. Individual kinetochores bind multiple microtubules. Anaphase B is modelled in a similar manner but in combination with the kinetochore and centriole which both have positive defect indexes whereby opposite spindle poles will also naturally move further away from each other because defects with indexes of the same sign repel. It may be the case for some cells, for example C. elegans, that anaphase A and anaphase B are overlapping events or that anaphase A is absent or of very short duration, as mentioned in the C. elegans example above. In this case the modelling should involve a three-body problem (see Eq. (A.19)) that combines the chromatid and kinetochore, MAP and centriole.

Throughout this work we have made the underlying assumption that the cells are spherical and because of this symmetry the two-dimensional defects we considered, which have regions of influence that are modelled as thin cylindrical discs sitting within the cell, provide an appropriate approximate modelling environment. However, normal eukaryotic cells are not spherical and although the ideas developed here are applicable to such cells it would be necessary to examine an extended theory applicable to three dimensional defects. Examples concerning the topology of defects in droplets can be found in [44]. The use of spherical micro-droplets of the nematic liquid crystal 5CB which contain central core point defects has been reviewed in [45] for use in the detection of keratin forming cell tumour line Type B (kB) cancer cells. These droplets interact with the KB cells (see [45, Fig. 5]) and the work we have presented here will be of value in exploring such interactions.

CRediT authorship contribution statement

Brian D. Sleeman: Writing – review & editing, Writing – original draft, Methodology, Formal analysis, Conceptualization. **Iain W. Stewart:** Writing – review & editing, Writing – original draft, Methodology, Formal analysis, Conceptualization.

Declaration of competing interest

The authors declared no competing interests.

Acknowledgements

The authors are indebted to Matthew A. Sleeman of Regeneron Pharmaceuticals, Inc. for his careful reading and helpful comments on an earlier draft of this paper. This work was inspired by the influential writings of John Lydon [10,43,46] in the Faculty of Biological Sciences, University of Leeds. It was these papers and my chance meeting with Professor Brian Sleeman in 2016 in Dundee which led us to embark on this project to understand the mechanisms which orchestrate the process of mitosis and animal cell division. This paper is dedicated to the memory of my co-author and friend, Professor Brian Sleeman, who sadly passed away in July 2021.

Funding acknowledgement

The authors received no financial support for the research, authorship, and/or publication of this article.

Appendix A. Defects and the interaction energy

The following is a précis of the form of interaction energy density for defects developed by Dafermos [23]. For convenience we use the standard notation (x_1, x_2) for Cartesian coordinates throughout this Appendix which derives the crucial polar coordinate forms of the interaction energies in Eqs. (A.18) and (A.19) below; it is especially (A.18) that we deploy in polar coordinates and so there should be no confusion between the final form of the energy used in Sections 4 and 5 and the notation for the time-dependent locations of the defects at $\mathbf{r}_1 = (x_1(t), 0)$ and $\mathbf{r}_2 = (0, x_2(t))$.

The director $\mathbf{n}$ is

$$\mathbf{n} = (\cos\theta, \sin\theta), \ \ \theta = \theta(x_1, x_2). \tag{A.1}$$

Under the one-constant approximation, the Frank–Oseen energy W from Eq. (4) per unit depth in z is given by

$$W = \frac{1}{2} K \int_{\Omega} \left(\theta_{x_1}^2 + \theta_{x_2}^2 \right) dx_1 dx_2, \tag{A.2}$$

and the corresponding Euler–Lagrange equation for equilibrium is

$$\theta_{x_1 x_1} + \theta_{x_2 x_2} = 0. \tag{A.3}$$

From (A.3) we see that the director alignment angle $\theta(x_1, x_2)$ satisfies Laplace's equation which when written in terms of the polar coordinates $x_1 = r\cos\phi$ and $x_2 = r\sin\phi$ becomes

$$\theta_{rr} + \frac{1}{r}\theta_r + \frac{1}{r^2}\theta_{\phi\phi} = 0. \tag{A.4}$$

For axial defects θ is independent of r and so

$$\theta = \frac{n}{2}\phi + \phi_0, \tag{A.5}$$

where ϕ_0 is an arbitrary constant angle and n, necessarily an integer by the symmetry of the director, is the *Frank index* of the defect. It is common to define the index I of the defect by $I \equiv n/2$; I is also called the strength of the defect and is often denoted by s in the general literature.

Flux lines are determined from geometric considerations as solutions of the nonlinear ordinary differential equation, in polar coordinates, given by (see [5,7] for details)

$$\frac{1}{r}\frac{dr}{d\phi} = \cot(\theta - \phi). \tag{A.6}$$

It is known that there are singular radial flux lines emanating from the origin and having direction determined by the relation

$$\theta - \phi = \mu\pi, \qquad \mu \text{ an integer}. \tag{A.7}$$

Employing the solution (A.5) for θ, the singular radial lines originate from the origin whenever

$$\phi = 2\frac{\mu\pi - \phi_0}{n-2}, \quad n \neq 2, \quad \mu \text{ an integer}. \tag{A.8}$$

The number of such lines is clearly $|n-2|$, that is, $|2(I-1)|$; there are therefore no singular radial lines when $I = +1$. For the case $n = 2$, (A.6) is easily solved to give the one parameter family

$$r = c\exp(\phi\cot\phi_0), \quad c \text{ a constant}. \tag{A.9}$$

For $n \neq 2$ Eq. (A.6) can be solved to obtain the one parameter family

$$r^{\frac{n}{2}-1} = C\sin\left(\left(\frac{n}{2} - 1\right)\phi + \phi_0\right), \quad C \text{ a constant}. \tag{A.10}$$

Examples of defects and flux lines for I equal to $+1$ and $+1/2$ at $\phi_0 = 0$ and for I equal to $-1/2$ at $\phi_0 = \pi/2$ are shown in Fig. 4. Further details, and a derivation and interpretation of the Frank index, can be found in [4,5,24].

We assume the cytoplasm Ω is smooth and simply connected and that on the boundary $\partial\Omega$, $\theta(x_1, x_2) = \theta_0(x_1, x_2)$ and follow the derivation in [23]. If the index $\mathbf{n}_0(x_1, x_2) = I \neq 0$, then $\theta_0(x_1, x_2)$ has a jump of $2\pi I$ at a point of $\partial\Omega$. Let $\mathbf{y}^1, \ldots, \mathbf{y}^N$ be a set of defect points in Ω and $\theta = \theta(x_1, x_2; \mathbf{y}^1, \ldots, \mathbf{y}^N)$ be an orientation pattern satisfying (A.3) on $\Omega - \{\mathbf{y}^1, \ldots, \mathbf{y}^N\}$ and the boundary condition and contains a disinclination of index I_i at $\mathbf{y}^i$, $i = 1, \ldots, N$. We note here, in the context of multiple defects, that Dafermos sets

$$I = \sum_{i=1}^{N} I_i\,. \tag{A.11}$$

Write

$$\theta(x_1, x_2; \mathbf{y}^1, \ldots, \mathbf{y}^N) = \sum_{i=1}^{N} \psi^i(x_1, x_2; \mathbf{y}^i) + \phi(x_1, x_2; \mathbf{y}^1, \ldots, \mathbf{y}^N), \tag{A.12}$$

where

$$\psi^i(x_1, x_2; \mathbf{y}^i) \equiv I_i \tan^{-1}\left(\frac{x_2 - y_2^i}{x_1 - y_1^i}\right), \tag{A.13}$$

and therefore $\phi(x_1, x_2; \mathbf{y}^1, \ldots, \mathbf{y}^N)$ is harmonic on $\Omega - \{\mathbf{y}^1, \ldots, \mathbf{y}^N\}$; for notational consistency with the other cited reviews in this paper, we have interchanged the notation for θ and ϕ that was originally used in [23]. As in [23], we can then write

$$\theta(x_1, x_2; \mathbf{y}^1, \ldots, \mathbf{y}^N) = \psi^i(x_1, x_2; \mathbf{y}^i) + \xi^i(x_1, x_2; \mathbf{y}^1, \ldots, \mathbf{y}^N), \tag{A.14}$$

$$\xi^i(x_1, x_2; \mathbf{y}^1, \ldots, \mathbf{y}^N) = \sum_{j \neq i} \psi^j(x_1, x_2; \mathbf{y}^j) + \phi(x_1, x_2; \mathbf{y}^1, \ldots, \mathbf{y}^N). \tag{A.15}$$

Then from (A.2) the energy density is $\frac{1}{2}K\omega$ where

$$\omega = I_i^2 r_i^{-2} + 2I_i r_i^{-1}\xi^i_{,2}\cos\chi^i - 2I_i r_i^{-1}\xi^i_{,1}\sin\chi^i + (\xi^i_{,1})^2 + (\xi^i_{,2})^2, \tag{A.16}$$

with a comma denoting partial differentiation with respect to the variable x_i, $i = 1, 2$ and, adopting the usual summation convention on j from 1 to 2,

$$r_i^2 \equiv (x_j - y_j^i)(x_j - y_j^i), \quad \chi^i \equiv \tan^{-1}\left(\frac{x_2 - y_2^i}{x_1 - y_1^i}\right), \quad i = 1, 2..., N. \tag{A.17}$$

The important example of (A.16) used extensively in this paper is for two defects when $N = 2$, given by

$$\omega = \frac{I_1^2}{r_1^2} + \frac{I_2^2}{r_2^2} + \frac{2I_1 I_2}{r_1 r_2}\cos(\chi^1 - \chi^2), \tag{A.18}$$

when harmonic contributions that would arise in the Euler–Lagrange equations are neglected. We record here, in an obvious notation, that for three simultaneous interacting defects

$$\omega = \frac{I_1^2}{r_1^2} + \frac{I_2^2}{r_2^2} + \frac{I_3^2}{r_3^2} + \frac{2I_1 I_2}{r_1 r_2}\cos(\chi^1 - \chi^2) + \frac{2I_1 I_3}{r_1 r_3}\cos(\chi^1 - \chi^3)$$

$$+\frac{2I_2I_3}{r_2r_3}\cos(\chi^2-\chi^3). \tag{A.19}$$

The analogue of (A.18) for any two defects can be obtained from (A.19) by setting the third defect index to zero.

Remark 1. There is an error in [23, Eqn.(4.16)] where the subscripts 1 and 2, corresponding to those in Eq. (A.16), should be interchanged.

Appendix B. Two-particle systems

Consider a two-particle system consisting of particles P_1 and P_2 with masses m_1 and m_2, respectively. It is known that the centre of mass of a two-particle system moves as a particle which has mass equal to the sum of the masses of the two particles and which is acted on by the sum of the external forces acting on the two particles. We now follow the notation and definitions in [47] and denote their position vectors relative to an arbitrary fixed origin $\mathbf{O}$ be $\mathbf{r}_1$ and $\mathbf{r}_2$, respectively. Let $\mathbf{F}_1^{\mathrm{int}}$ denote the internal force that acts on P_1 due to P_2 with an analogous definition for $\mathbf{F}_2^{\mathrm{int}}$ for the force that acts on P_2 due to P_1; as is well known, from Newton's third law of motion, the sum of these internal forces is zero and so $\mathbf{F}_2^{\mathrm{int}} = -\mathbf{F}_1^{\mathrm{int}}$. Let $\mathbf{F}_1^{\mathrm{ext}}$ and $\mathbf{F}_2^{\mathrm{ext}}$ denote the external forces acting on P_1 and P_2 respectively, due to influences outside the two-particle system. From Newton's second law of motion, the equations of motion for these particles can be written as

$$m_1\ddot{\mathbf{r}}_1 = \mathbf{F}_1^{\mathrm{int}} + \mathbf{F}_1^{\mathrm{ext}}, \tag{B.1}$$

$$m_2\ddot{\mathbf{r}}_2 = \mathbf{F}_2^{\mathrm{int}} + \mathbf{F}_2^{\mathrm{ext}}, \tag{B.2}$$

where a superposed dot represents the derivative with respect to time t. Adding these two equations clearly gives the equation of motion for the centre of mass with position vector $\mathbf{R}$ defined by

$$\mathbf{R} = \frac{1}{m}\left(m_1\mathbf{r}_1 + m_2\mathbf{r}_2\right), \tag{B.3}$$

where $m = m_1 + m_2$.

Now set $\mathbf{r} = \mathbf{r}_1 - \mathbf{r}_2$. Then, from Eqs. (B.1) and (B.2),

$$\begin{aligned}\ddot{\mathbf{r}} &= \frac{\mathbf{F}_1^{\mathrm{int}}}{m_1} - \frac{\mathbf{F}_2^{\mathrm{int}}}{m_2} + \frac{\mathbf{F}_1^{\mathrm{ext}}}{m_1} - \frac{\mathbf{F}_2^{\mathrm{ext}}}{m_2}\\ &= \frac{m}{m_1m_2}\mathbf{F}_1^{\mathrm{int}} + \frac{\mathbf{F}_1^{\mathrm{ext}}}{m_1} - \frac{\mathbf{F}_2^{\mathrm{ext}}}{m_2},\end{aligned} \tag{B.4}$$

which can be written in the form

$$\mu\ddot{\mathbf{r}} = \mathbf{F}_1^{\mathrm{int}} + \frac{1}{m}\left(m_2\mathbf{F}_1^{\mathrm{ext}} - m_1\mathbf{F}_2^{\mathrm{ext}}\right), \tag{B.5}$$

where μ denotes the reduced mass of the system, defined by

$$\mu = \frac{m_1m_2}{m}. \tag{B.6}$$

The two-particle system (B.1) and (B.2) can be solved numerically for general internal and external forces, but a simplification to a system of two equations of motions for two one-particle systems is possible under some basic modelling assumptions. This will allow us to gain insight to the structure of the problem. It can be supposed, for our purposes, that $\mathbf{F}_1^{\mathrm{ext}}$ and $\mathbf{F}_2^{\mathrm{ext}}$ are drag forces of the forms

$$\mathbf{F}_1^{\mathrm{ext}} = -\xi_1\dot{\mathbf{r}}_1, \qquad \mathbf{F}_2^{\mathrm{ext}} = -\xi_2\dot{\mathbf{r}}_2, \tag{B.7}$$

where ξ_1 and ξ_2 are coefficients with dimensions of mass divided by time; it is well known that each of these coefficients depends on the geometric shape of the individual particle and the material parameters of the system under consideration (cf. [48, Sections 4.9 &4.10]). Under the approximation

$$m_2\xi_1 = m_1\xi_2, \tag{B.8}$$

which is effectively a supposed relationship between the coefficients and the particle masses, Eq. (B.5) becomes

$$\mu\ddot{\mathbf{r}} = \mathbf{F}_1^{\mathrm{int}} - \xi\dot{\mathbf{r}}, \tag{B.9}$$

where $\mathbf{F}_1^{\mathrm{int}}$ is now expressed as a function of $\mathbf{r}$ and ξ is introduced as the reduced coefficient, defined here by

$$\xi \equiv \frac{m_2}{m}\xi_1 = \frac{m_1}{m}\xi_2. \tag{B.10}$$

Further, a straightforward calculation shows that the equation of motion for the centre of mass is then described by

$$\ddot{\mathbf{R}} = -\lambda_1\dot{\mathbf{R}}, \qquad \lambda_1 = \frac{\xi_1}{m_1}. \tag{B.11}$$

Consequently, the original two-particle system in Eqs. (B.1) and (B.2) is equivalent to the system

$$\ddot{\mathbf{R}} = -\lambda_1\dot{\mathbf{R}}, \tag{B.12}$$

$$\mu\ddot{\mathbf{r}} = \mathbf{F}_1^{\mathrm{int}} - \xi\dot{\mathbf{r}}. \tag{B.13}$$

This transformed system now consists of two equations of motion for two one-particle systems. Eq. (B.12) is an equation of motion for the centre of mass under the influence of an external force which is the same as that acting per unit mass on the particles P_1 and P_2. Eq. (B.13) describes the motion of a fictitious particle of mass μ under the influence of the internal force $\mathbf{F}_1^{\mathrm{int}}$ acting on the particle P_1 with coefficient ξ. Eq. (B.12) is readily solved to find that

$$\mathbf{R}(t) = \lambda_1^{-1}\left(1 - e^{-\lambda_1 t}\right)\dot{\mathbf{R}}(0) + \mathbf{R}(0), \tag{B.14}$$

with prescribed initial conditions $\dot{\mathbf{R}}(0)$ and $\mathbf{R}(0)$ which are, of course, determined by the initial conditions for particles P_1 and P_2. Notice that if the initial velocities of these particles are zero then the centre of mass of the two-particle system remains fixed at $\mathbf{R}(0)$. Once Eq. (B.13) has been solved for $\mathbf{r}(t)$ then the solution to the original system can be determined from (B.3) (e.g., replace $\mathbf{r}_1$ by $\mathbf{r} + \mathbf{r}_2$) as

$$\mathbf{r}_1(t) = \mathbf{R}(t) + \frac{m_2}{m}\mathbf{r}(t), \tag{B.15}$$

$$\mathbf{r}_2(t) = \mathbf{R}(t) - \frac{m_1}{m}\mathbf{r}(t), \tag{B.16}$$

which provides the positions for the particles P_1 and P_2 relative to the original fixed origin. We also note here that in the absence of drag forces these equations reduce to the classical forms [47]

$$\ddot{\mathbf{R}} = \mathbf{0}, \tag{B.17}$$

$$\mu\ddot{\mathbf{r}} = \mathbf{F}_1^{\mathrm{int}}. \tag{B.18}$$

Appendix C. Interaction energy and force: special case

We give an example here of an exact integral for the interaction energy that is available in the special case of two interacting defects when $R_1 + r_0 \le d \le R_2 - R_1$, including the consequent explicit function for the force of interaction. Consider two defects of indexes I_1 and I_2 with associated regions of influence R_1 and R_2, respectively, and that the circle R_1 is completely contained within the circle R_2 and has no overlap with the core defect located at the centre of circle R_2, that is, we assume that $R_1 + r_0 \le d \le R_2 - R_1$. Let the corresponding defects be positioned at $(x_1, 0)$ and $(x_2, 0)$ and set $d = (x_1 - x_2)$. Relative to a fixed origin in the xy-plane we write $x = r\cos\theta + x_1$, $y = r\sin\theta$. The regions of influence are the circles defined by $R_i^2 = (x - x_i)^2 + y^2$, $i = 1, 2$. Using the definitions in Eqs. (A.17) and (A.18) from Appendix A, the interaction energy density is

$$\omega = \frac{I_1^2}{r_1^2} + \frac{I_2^2}{r_2^2} + \frac{2I_1I_2}{r_1r_2}\cos(\chi^1 - \chi^2), \tag{C.1}$$

which can be written as

$$\omega = \frac{I_1^2}{r^2} + \frac{I_2^2}{r^2 + 2rd\cos\theta + d^2} + \frac{2I_1I_2\cos(\chi^1 - \chi^2)}{r(r^2 + 2rd\cos\theta + d^2)^{1/2}}, \tag{C.2}$$

where

$$\cos(\chi^1 - \chi^2) = \frac{r_1^2 + r_2^2 - d^2}{2r_1r_2} = \frac{(r + d\cos\theta)}{(r^2 + 2rd\cos\theta + d^2)^{1/2}}. \tag{C.3}$$

The total energy is

$$W = \frac{1}{2}K\int_0^{2\pi}\int_{r_0}^{R_1} \omega r dr d\theta \equiv W_1 + W_2 + W_3, \tag{C.4}$$

where

$$W_1 = \pi K I_1^2 \int_{r_0}^{R_1} \frac{dr}{r} = \pi K I_1^2 \ln\left(\frac{R_1}{r_0}\right), \tag{C.5}$$

$$W_2 = \frac{1}{2}K I_2^2 \int_0^{2\pi}\int_{r_0}^{R_1} \frac{r dr d\theta}{(r^2 + 2rd\cos\theta + d^2)} = -\frac{1}{2}K\pi I_2^2 \ln\left(\frac{d^2 - R_1^2}{d^2 - r_0^2}\right), \tag{C.6}$$

and

$$\begin{aligned} W_3 &= K I_1 I_2 \int_0^{2\pi}\int_{r_0}^{R_1} \frac{(r + d\cos\theta)}{(r^2 + 2rd\cos\theta + d^2)} dr d\theta \\ &= \frac{1}{2}K I_1 I_2 \int_0^{2\pi} \ln\left[\frac{R_1^2 + 2R_1 d\cos\theta + d^2}{r_0^2 + 2r_0 d\cos\theta + d^2}\right] d\theta \\ &= \frac{1}{2}K I_1 I_2 \int_0^{2\pi} \ln\left[\frac{1 + 2(R_1/d)\cos\theta + (R_1/d)^2}{1 + 2(r_0/d)\cos\theta + (r_0/d)^2}\right] d\theta. \end{aligned} \tag{C.7}$$

Using the identity [49, 4.224.15]

$$\int_0^{n\pi} \ln(1 - 2a\cos\theta + a^2) d\theta = \begin{cases} 0 & \text{if } a^2 \le 1, \\ n\pi \ln a^2 & \text{if } a^2 > 1, \end{cases} \tag{C.8}$$

we find that $W_3 = 0$ for the range of interest here where $R_1 + r_0 \le d \le R_2 - R_1$. Hence the interaction energy in this special case is (per unit depth in the z-direction)

$$W = \pi K I_1^2 \ln\left(\frac{R_1}{r_0}\right) - \frac{1}{2}K\pi I_2^2 \ln\left(\frac{d^2 - R_1^2}{d^2 - r_0^2}\right), \tag{C.9}$$

which has been used for a comparison with the numerically derived interaction energies in Figs. 7(a) and 9(a) for $R_1 + r_0 \le d \le R_2 - R_1$ and, analogously, Figs. 7(c) and 9(c) for $R_2 + r_0 \le d \le R_3 - R_2$, which gives confidence in the numerical procedure outlined in Section 4. Numerical evaluations of the integrals are required for values of d outside this range.

Remark 2. Note that if $2r_0 < d < R_1 + r_0$ then, although the region of integration will change (it will overlap with the I_1 defect core) $W_3 \simeq 2K\pi I_1 I_2 \ln(R_1/d)$ per unit depth in the z-direction, obtained from Eqs. (C.7) and (C.8) and this gives rise to a corresponding contributing force per unit depth of $F = -\mathrm{d}W_3/\mathrm{d}d \simeq 2K\pi I_1 I_2/d$ which is negative when I_1 and I_2 have opposite signs. This indicates an attractive force F between the defects. This form for F coincides with an expression in [4, p. 173] if $I_1 = -I_2 \equiv m$ where m is the magnitude of their strengths and R_1 is taken to be much larger than d. See also [15, p. 428].

References

[1] B. Alberts, A. Johnson, J. Lewis, D. Morgan, M. Raff, K. Roberts, P. Walter, Molecular Biology of the Cell, sixth ed., Garland Science, New York, 2015.

[2] D. Dunmur, T. Sluckin, Soap, Science and Flat-Screen TVs: A History of Liquid Crystals, Oxford University Press, Inc., New York, 2011.

[3] S. Chandrasekhar, Liquid Crystals, second ed., Cambridge University Press, Cambridge, 1992, http://dx.doi.org/10.1017/CBO9780511622496.

[4] P.G. de Gennes, J. Prost, The Physics of Liquid Crystals, second ed., Oxford University Press, Oxford, 1993, http://dx.doi.org/10.1093/oso/9780198520245.001.0001.

[5] I.W. Stewart, The Static and Dynamic Continuum Theory of Liquid Crystals, Taylor and Francis, London and New York, 2004, http://dx.doi.org/10.1201/9781315272580.

[6] E.G. Virga, Variational Theories for Liquid Crystals, Chapman and Hall, London, 1994, http://dx.doi.org/10.1201/9780203734421.

[7] M.J. Stephen, J.P. Straley, Physics of liquid crystals, Rev. Modern Phys. 46 (1974) 617–704, http://dx.doi.org/10.1103/RevModPhys.46.617.

[8] J.W. Goodby, P.J. Collings, T. Kato, C. Tschierske, H.F. Gleeson, P. Raynes, V. Vill, Handbook of Liquid Crystals, 8 Volume Set, Vol. 1, John Wiley & Sons, 2014, http://dx.doi.org/10.1002/9783527671403.

[9] B. Alberts, D. Bray, J. Lewis, M. Raff, K. Roberts, J.D. Watson, Molecular Biology of the Cell, Garland Publishing, Inc., New York, 1983.

[10] J. Lydon, Microtubules: Nature's smartest mesogens – a liquid crystal model for cell division, Liq. Cryst. Today 15 (2) (2006) 1–10, http://dx.doi.org/10.1080/14645180600916367.

[11] C.M. O'Connor, J.U. Adams, Essentials of Cell Biology, NPG Education, Cambridge, MA, 2010, URL https://www.nature.com/scitable/ebooks/essentials-of-cell-biology-14749010.

[12] T. Fukagawa, P. De Wulf, Kinetochore composition, formation, and organization, in: P. De Wulf, W.C. Earnshaw (Eds.), The Kinetochore, Springer, New York, 2009, pp. 133–191, http://dx.doi.org/10.1007/978-0-387-69076-6_6, Ch. 6.

[13] L.J. Fulcher, Z. He, L. Mei, T.J. Macartney, N.T. Wood, A.R. Prescott, A.J. Whigham, J. Varghese, R. Gourlay, G. Ball, R. Clarke, D.G. Campbell, C.A. Maxwell, G.P. Sapkota, FAM83D directs protein kinase CK1α to the mitotic spindle for proper spindle positioning, EMBO Rep. 20 (9) (2019) e47495, http://dx.doi.org/10.1101/480616.

[14] L.T. Ferreira, B. Orr, G. Rajendraprasad, A.J. Pereira, C. Lemos, J.T. Lima, C. Guasch Boldú, J.G. Ferreira, M. Barisic, H. Maiato, α-Tubulin detyrosination impairs mitotic error correction by suppressing MCAK centromeric activity, J. Cell Biol. 219 (4) (2020) http://dx.doi.org/10.1083/jcb.201910064.

[15] M. Kléman, O.D. Lavrentovich, Soft Matter Physics: An Introduction, Springer-Verlag, New York, 2003, http://dx.doi.org/10.1007/b97416.

[16] I. Newton, Opticks, fourth ed., William Innys, London, 1730.

[17] K. Kawaguchi, R. Kageyama, M. Sano, Topological defects control collective dynamics in neural progenitor cell cultures, Nature 545 (7654) (2017) 327–331, http://dx.doi.org/10.1038/nature22321.

[18] T.B. Saw, A. Doostmohammadi, V. Nier, L. Kocgozlu, S. Thampi, Y. Toyama, P. Marcq, C.T. Lim, J.M. Yeomans, B. Ladoux, Topological defects in epithelia govern cell death and extrusion, Nature 544 (7649) (2017) 212–216, http://dx.doi.org/10.1038/nature21718.

[19] L.S. Hirst, G. Charras, Liquid crystals in living tissue, Nature 544 (7649) (2017) 164–165, http://dx.doi.org/10.1038/544164a.

[20] M. Leoni, O.V. Manyuhina, M.J. Bowick, M.C. Marchetti, Defect driven shapes in nematic droplets: analogies with cell division, Soft Matter 13 (6) (2017) 1257–1266, http://dx.doi.org/10.1039/c6sm02584f.

[21] A. Mogilner, R. Wollman, G. Civelekoglu-Scholey, J. Scholey, Modeling mitosis, Trends Cell Biol. 16 (2) (2006) 88–96, http://dx.doi.org/10.1016/j.tcb.2005.12.007.

[22] A. Doostmohammadi, B. Ladoux, Physics of liquid crystals in cell biology, Trends Cell Biol. 32 (2) (2022) 140–150, http://dx.doi.org/10.1016/j.tcb.2021.09.012.

[23] C.M. Dafermos, Disinclinations in liquid crystals, Q. J. Mech. Appl. Math. 23 (2) (1970) S49–S64, http://dx.doi.org/10.1093/qjmam/23.2.49.

[24] F.C. Frank, On the theory of liquid crystals, Discuss. Faraday Soc. 25 (1958) 19–28, http://dx.doi.org/10.1039/DF9582500019.

[25] J.V. Selinger, Introduction to the Theory of Soft Matter: From Ideal Gases to Liquid Crystals, Springer, New York, 2016, http://dx.doi.org/10.1007/978-3-319-21054-4.

[26] J.D. Eshelby, The force on a disclination in a liquid crystal, Philos. Mag. A 42 (3) (1980) 359–367, http://dx.doi.org/10.1080/01418618008239363.

[27] Maple 2021, ODE Solver, Waterloo Maple Inc., 2021.

[28] OriginPro, Version 2021b, OriginLab Corporation, 2021.

[29] A. Piovesan, M.C. Pelleri, F. Antonaros, P. Strippoli, M. Caracausi, L. Vitale, On the length, weight and GC content of the human genome, BMC Res. Notes 12 (1) (2019) 1–7, http://dx.doi.org/10.1186/s13104-019-4137-z.

[30] D.H. Boal, Mechanics of the Cell, second ed., Cambridge University Press, New York, 2012, http://dx.doi.org/10.1017/CBO9781139022217.

[31] K.-C. Su, Z. Barry, N. Schweizer, H. Maiato, M. Bathe, I.M. Cheeseman, A regulatory switch alters chromosome motions at the metaphase-to-anaphase transition, Cell Rep. 17 (7) (2016) 1728–1738, http://dx.doi.org/10.1016/j.celrep.2016.10.046.

[32] K. Vukušić, R. Buda, I.M. Tolić, Force-generating mechanisms of anaphase in human cells, J. Cell Sci. 132 (18) (2019) jcs231985, http://dx.doi.org/10.1242/jcs.231985.

[33] K. Bloom, The centromere frontier: kinetochore components, microtubule-based motility, and the CEN-value paradox, Cell 73 (4) (1993) 621–624, http://dx.doi.org/10.1016/0092-8674(93)90242-I.

[34] P. Meraldi, V.M. Draviam, P.K. Sorger, Timing and checkpoints in the regulation of mitotic progression, Dev. Cell 7 (1) (2004) 45–60, http://dx.doi.org/10.1016/j.devcel.2004.06.006.

[35] D.G. Albertson, J.N. Thomson, The kinetochores of caenorhabditis elegans, Chromosoma 86 (3) (1982) 409–428, http://dx.doi.org/10.1007/BF00292267.

[36] J.-C. Labbé, E.K. McCarthy, B. Goldstein, The forces that position a mitotic spindle asymmetrically are tethered until after the time of spindle assembly, J. Cell Biol. 167 (2) (2004) 245–256, http://dx.doi.org/10.1083/jcb.200406008.

[37] L. Pintard, B. Bowerman, Mitotic cell division in caenorhabditis elegans, Genetics 211 (1) (2019) 35–73, http://dx.doi.org/10.1534/genetics.118.301367.

[38] J. Spieth, D. Lawson, P. Davis, G. Williams, K. Howe, Overview of Gene Structure in C. Elegans, WormBook, 2014, http://dx.doi.org/10.1895/wormbook.1.65.2.

[39] J.E. Sulston, S. Brenner, The DNA of caenorhabditis elegans, Genetics 77 (1) (1974) 95–104, http://dx.doi.org/10.1093/genetics/77.1.95.

[40] M.D. Betterton, J.R. McIntosh, Regulation of chromosome speeds in mitosis, Cell. Mol. Bioeng. 6 (4) (2013) 418–430, http://dx.doi.org/10.1007/s12195-013-0297-4.

[41] C.W. Oseen, The theory of liquid crystals, Trans. Faraday Soc. 29 (1933) 883–899, http://dx.doi.org/10.1039/TF9332900883.

[42] D. Miroshnychenko, N.A. Hill, N.J. Mottram, J.E. Lydon, Liquid crystal pre-patterning in mitosis, in: Proceedings of the 2005 Summer Bioengineering Conference, June 22-26, Vail Cascade Resort & Spa, Vail, Colorado, USA, 2005, pp. 415–416.

[43] J. Lydon, Microtubules–nature's universal mesogens, Mol. Cryst. Liq. Cryst. 632 (1) (2016) 29–48, http://dx.doi.org/10.1080/15421406.2016.1185569.

[44] O.D. Lavrentovich, Topological defects in dispersed words and worlds around liquid crystals, or liquid crystal drops, Liq. Cryst. 24 (1) (1998) 117–126, http://dx.doi.org/10.1080/026782998207640.

[45] J. Vallamkondu, E.B. Corgiat, G. Buchaiah, R. Kandimalla, P.H. Reddy, Liquid crystals: A novel approach for cancer detection and treatment, Cancers 10 (11) (2018) 462, http://dx.doi.org/10.3390/cancers10110462.

[46] J.E. Lydon, A liquid crystal model for mitotic cell division - and the enigma of centriole involvement in mitosis in animals but not plants, Liq. Cryst. Today 28 (4) (2019) 86–95, http://dx.doi.org/10.1080/1358314X.2020.1726065.

[47] H.C. Corben, P. Stehle, Classical Mechanics, second ed., John Wiley & Sons, Inc., 1960.

[48] G.K. Batchelor, An Introduction to Fluid Dynamics, Cambridge University Press, Cambridge, 2000, http://dx.doi.org/10.1017/CBO9780511800955.

[49] I.S. Gradshteyn, I.M. Ryzhik, Table of Integrals, Series and Products, seventh ed., Academic Press, San Diego, 2007.